

# Massive Star Clusters in the Semi-Analytical Galaxy Formation Model *L-Galaxies* 2020

Nils Hoyer<sup>1,2,3</sup>, Silvia Bonoli<sup>1,4</sup>, Nate Bastian<sup>1,4</sup>, Diego Herrero-Carrión<sup>1</sup>, Nadine Neumayer<sup>2</sup>, David Izquierdo-Villalba<sup>5,6</sup>, Daniele Spinoso<sup>7</sup>, Robert M. Yates<sup>8</sup>, Markos Polkas<sup>1,9</sup>, and M. Celeste Artale<sup>10</sup>

<sup>1</sup> Donostia International Physics Center, Paseo Manuel de Lardizabal 4, E-20118 Donostia-San Sebastián, Spain

<sup>2</sup> Max-Planck-Institut für Astronomie, Königstuhl 17, D-69117 Heidelberg, Germany  
e-mail: [hoyer@mpia.de](mailto:hoyer@mpia.de)

<sup>3</sup> Universität Heidelberg, Seminarstrasse 2, D-69117 Heidelberg, Germany

<sup>4</sup> Ikerbasque, Basque Foundation for Science, E-48013 Bilbao, Spain

<sup>5</sup> Dipartimento di Fisica “G. Occhialini”, Università degli Studi di Milano-Bicocca, Piazza della Scienza 3, 20126 Milano, Italy

<sup>6</sup> INFN, Sezione di Milano-Bicocca, Piazza della Scienza 3, 20126 Milano, Italy

<sup>7</sup> Department of Astronomy, Tsinghua University, Beijing 100084, China

<sup>8</sup> Centre for Astrophysics Research, University of Hertfordshire, Hatfield, AL10 9AB, United Kingdom

<sup>9</sup> University of the Basque Country UPV/EHU, Department of Theoretical Physics, Bilbao, E-48080, Spain

<sup>10</sup> Departamento de Ciencias Físicas, Facultad de Ciencias Exactas, Universidad Andres Bello, Fernández Concha 700, Las Condes, Santiago, Chile

Received 28 Feb, 2025; accepted xx yy, 2025

## ABSTRACT

It is established that there exists a direct link between the formation history of star cluster populations and their host galaxies, however, our lacking understanding of star cluster assembly prohibits us to make full use of their ability to trace galaxy evolution. In this work we introduce a new variation of the 2020 version of the semi-analytical galaxy formation model “*L-Galaxies*” that includes the formation of star clusters above  $10^3 M_{\odot}$  and probes different physical assumptions that affect their evolution over cosmic time. We use properties of different galaxy components and localised star formation to determine the bound fraction of star formation in disks. After randomly sampling masses from an environmentally-dependent star cluster initial mass function, we assign to each object a half-mass radius, metallicity, and distance from the galaxy centre. We consider up to 2000 individual star clusters per galaxy and evolve their properties over time taking into account stellar evolution, two-body relaxation, tidal shocks, dynamical friction, and a re-positioning during galaxy mergers. Our simulation successfully reproduces several observational quantities, such as the empirical relationship between the absolute *V*-band magnitude of the brightest young star clusters and the host galaxy star formation rate, the mass function of young star clusters, or mean metallicities of the star cluster distributions versus galaxy masses. The simulation reveals great complexity in the  $z = 0$  star cluster population resulting from differential destruction channels and origins, including *in-situ* populations in the disk, a major merger-induced heated component in the halo, and accreted star clusters. Model variations point out the importance of e.g. the shape of the star cluster initial mass function or the relationship between the sound speed of cold gas and the star formation rate. Our new model provides new avenues to trace individual star clusters and test cluster-related physics within a cosmological set-up in a computationally efficient manner.

**Key words.** Galaxies: star clusters: general – Methods: numerical

## 1. Introduction

A natural consequence of star formation in cold gas-dense and rotationally unstable regions is the formation of bound stellar structures, ranging from few-body systems to massive star clusters that rival in mass the baryonic components of entire (dwarf) galaxies. The properties and survival times of these star clusters heavily depend on their changing environment, which makes them excellent tracers of galaxy assembly. To date, a large body of work has used the present-day star cluster population, such as globular clusters, to constrain the evolutionary history of their current host galaxy, including the Milky Way, M31, and other nearby systems (e.g. Huchra et al. 1991; Barmby et al. 2000; Perrett et al. 2002;

West et al. 2004; Brodie & Strader 2006; Forbes & Bridges 2010; Leaman et al. 2013; Huxor et al. 2014; Cantiello et al. 2015; Veljanoski et al. 2015; Myeong et al. 2018; Callingham et al. 2022; Hammer et al. 2023, 2024; Ines Ennis et al. 2024; Usher et al. 2024). However, despite the clear link between galaxy and star cluster formation that is expressed via, for example, the scaling relation between the number of star clusters and host galaxy mass (e.g. West et al. 1995; Blakeslee 1999; Peng et al. 2008; Spitler & Forbes 2009; Hudson et al. 2014; El-Badry et al. 2019; Bastian et al. 2020; Burkert & Forbes 2020; Zaritsky 2022; Le & Cooper 2024), precise details about the formation environments and initial properties of  $z = 0$  star clusters remain elusive (e.g. Forbes et al. 2018).

Constraints on the ages of globular clusters in galaxies, including the Milky Way, suggest that they form at redshifts  $z \gtrsim 1$  (e.g. Carretta et al. 2000; Krauss & Chaboyer 2003; Lee 2003; Kaviraj et al. 2005; Strader et al. 2005; Correnti et al. 2016). Studying the natal environment of clusters at these distances is challenging; however, observations with the *Very Large Telescope*, the *Hubble Space Telescope*, and *James Webb Space Telescope*, combined with strong gravitational lensing, make such observations possible (e.g. Vanzella et al. 2017, 2019; Kikuchihara et al. 2020; Mowla et al. 2022; Forbes & Romanowsky 2023; Vanzella et al. 2023; Claeysens et al. 2023; Mowla et al. 2024). Most recently, Adamo et al. (2024) discussed the properties of young and massive star clusters in the “Cosmic Gems Arc” at redshift  $z \approx 10$  (Salmon et al. 2018; Bradley et al. 2024). Such clusters are compact (half-light radius  $\leq 2$  pc), massive (stellar mass  $\gtrsim 10^6 M_\odot$ ), and could potentially contribute to the  $z = 0$  star cluster population. Irrespective of whether they survive until  $z = 0$ , they constitute a significant baryonic component of high- $z$  galaxies ( $\gtrsim 30\%$  for the Cosmic Gems Arc; Adamo et al. 2024) and most likely influence the host galaxy’s evolution.

Simulations are required to understand the properties of the full star cluster distribution as observations can only trace the brightest / most massive and most unobscured star clusters. Detailed simulations of star cluster formation and evolution have now become feasible in high-resolution hydrodynamical simulations of galaxy formation, ranging from dwarf galaxies to Milky Way analogues. These simulations either include star clusters in full cosmological simulations, sometimes including adaptive mesh-refinement or zoom-in techniques (e.g. Li et al. 2017, 2018; Li & Gnedin 2019; Brown & Gnedin 2022; Reina-Campos et al. 2022a; Garcia et al. 2023; Calura et al. 2024) or use high spatial- and temporal resolutions but evolve for less than one Gyr (e.g. Lahén et al. 2020; Hislop et al. 2022; Lahén et al. 2023; Elmegreen & Lahén 2024; Lahén et al. 2024a,b; Reina-Campos et al. 2024). Another approach is to add star cluster-related physics to existing simulations. This approach was realised by e.g. the *E-MOSAICS* project (Pfeffer et al. 2018; Kruijssen et al. 2019a) that adds prescriptions for star cluster formation in post-processing to the *EAGLE* simulation (Crain et al. 2015; Schaye et al. 2015). Focussing on *E-MOSAICS*, their simulation can reproduce a number of observables related to the globular clusters mass and metallicity distributions as well as relations with properties of their host galaxy and dark matter halo (see details in Hughes et al. 2019; Kruijssen et al. 2019a,b; Reina-Campos et al. 2019; Pfeffer et al. 2019a,b; Bastian et al. 2020; Hughes et al. 2020; Kruijssen et al. 2020; Reina-Campos et al. 2020; Keller et al. 2020; Horta et al. 2011; Trujillo-Gomez et al. 2021; Dolfi et al. 2022; Hughes et al. 2022; Reina-Campos et al. 2022b, 2023b; Newton et al. 2024; Pfeffer et al. 2024b,a).

All of the above mentioned simulations follow in detail the evolution of stars within individual star clusters or of individual baryonic particles, which contain star clusters, but are expensive to run. In contrast, semi-analytical models sacrifice resolution to lower the computational expense and gain the ability to explore a wide parameter space of various astrophysical mechanisms (e.g. White & Rees 1978; White & Frenk 1991; Baugh 2006; Somerville et al. 2008; Somerville & Davé 2015). This approach has proven to be successful in reproducing observational quantities related to, for example, the co-evolution of galaxies and massive black holes (e.g. Kauffmann & Haehnelt 2000; Croton et al.

2006; Croton 2006; De Lucia & Blaizot 2007; Monaco et al. 2007; Bonoli et al. 2009, 2014; Izquierdo-Villalba et al. 2020; Gabrielpillai et al. 2022; del P. Lagos et al. 2024), which allows to constrain values of free parameters of the assumed physical models.

For star clusters in a semi-analytical galaxy formation framework specifically, most recently De Lucia et al. (2024) added prescriptions for their formation to the *GAEA* model (De Lucia et al. 2014; Hirschmann et al. 2016). The authors were able to reproduce the empirical relationship between the total mass in globular clusters and the parent halo mass (see also e.g. Kravtsov & Gnedin 2005; Prieto & Gnedin 2008; Muratov & Gnedin 2010; Li et al. 2017) but utilised simple prescriptions related to mass loss and dynamical friction and relied on global star cluster population statistics.

In this first paper, we introduce an implementation of the formation and evolution of star clusters into a public version of the semi-analytical galaxy formation model “*L-Galaxies*” (Henriques et al. 2020; Yates et al. 2021). Our work differs from the above mentioned work by De Lucia et al. (2024) in that we track the evolution of individual clusters and use different sets of astrophysical prescriptions that make use of the radially-resolved gas and stellar discs in the 2020 version of the code. This effort enables us to study individual star clusters across different galaxy types, masses, environments, and redshifts, and offers new avenues to study the formation of nuclear star clusters and the co-evolution of black holes with star clusters in future work.

We start in Section 2 by detailing the governing equations of the model, starting with galaxy components to evaluate the formation efficiency of star clusters, the initial properties of the star clusters, and eventually the evolution of star clusters within the evolution of their host galaxies. We then evaluate results of our model in Section 3 focussing on young massive star clusters in disk-dominated galaxies, and metallicity distributions of *in-situ* and accreted star clusters for different galaxy morphologies, and discuss caveats of our approach. We conclude in Section 4 and present an outlook for future papers in this series. Appendix A presents variations of key model parameters.

## 2. Model description

Below we outline the basic principles behind our model that we summarise in Figure 1. Going forward, when mentioning the term *L-Galaxies* we specifically refer to a modified version of the 2020 model introduced by Yates et al. (2021). This version of the code improves over the default model (Henriques et al. 2020) by modifying the prescriptions for metal injection from stellar winds and supernovae into the circum-galactic medium.

### 2.1. The *L-Galaxies* semi-analytical galaxy formation model

The *L-Galaxies* model combines merger trees from dark matter-only  $N$ -body simulations with a set of partial differential equations for the evolution of baryonic components. It has been developed to primarily run on the Millennium (Springel et al. 2005) and Millennium-II (Boylan-Kolchin et al. 2009) simulations with box sizes / dark matter particle masses of  $480.3 h^{-1} \text{Mpc} / 9.61 \times 10^8 h^{-1} M_\odot$  and  $96.1 h^{-1} \text{Mpc} / 7.69 \times 10^6 h^{-1} M_\odot$ , respectively. Dark matter (sub-)halos are identified using a “Friends-of-Friends” (Davis et al. 1985)

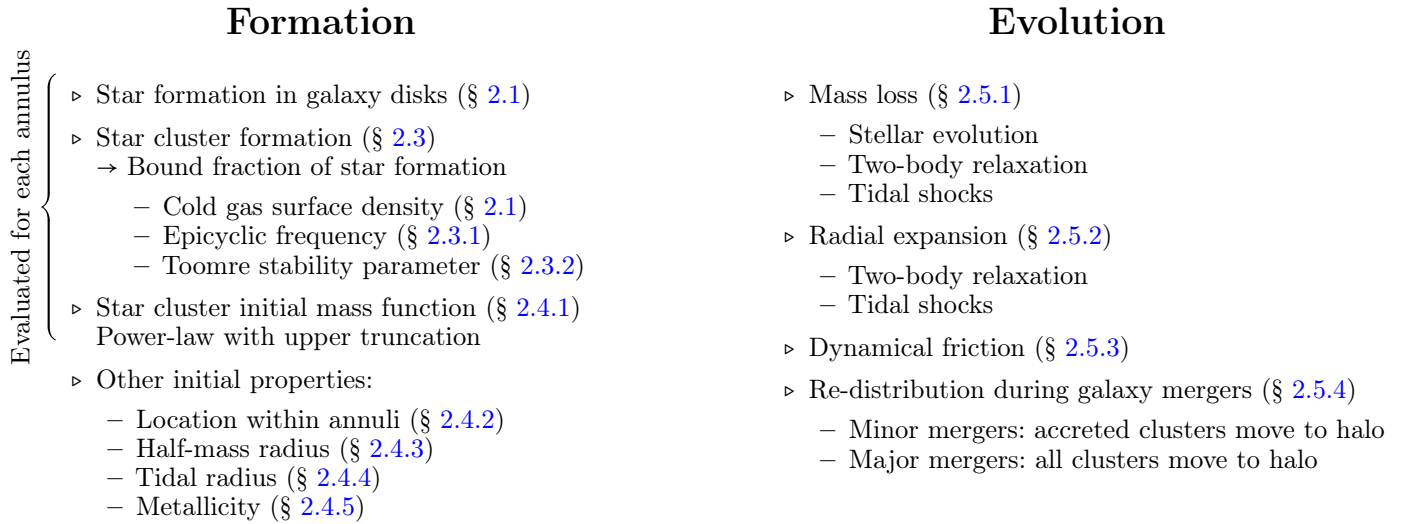


Fig. 1: Relevant prescriptions for the assembly of star clusters implemented into a modified version (Yates et al. 2021) of *L-Galaxies* 2020 (Henriques et al. 2020).

and the “subfind” algorithm (Springel et al. 2001; Dolag et al. 2009) and are used as input to *L-Galaxies*. As discussed in the works related to the last few major releases (Guo et al. 2011; Henriques et al. 2015, 2020), the model can reproduce many observables of baryonic components, such as the redshift-dependent galaxy mass function, passive galaxy fraction, and the cosmic density of the star formation rate (SFR).

Many extensions to *L-Galaxies* have been developed, including those that focus on the gas (Vijayan et al. 2019; Ayromlou et al. 2021; Yates et al. 2021; Parente et al. 2023; Zhong et al. 2023a,b; Parente et al. 2024; Yates et al. 2024), stars (Bluck et al. 2016; Wang et al. 2018; Irodoutou et al. 2019; Izquierdo-Villalba et al. 2019; Murphy et al. 2022; Wang & Peng 2024), massive black holes (Bonoli et al. 2009, 2014; Izquierdo-Villalba et al. 2020, 2022; Spinoso et al. 2023; Polkas et al. 2024), and other components (Barrera et al. 2023; Vani et al. 2025). This shows that *L-Galaxies* is a versatile utility to explore the assembly of galaxies and has the potential to investigate the formation of star clusters as well.

One of the key features of the 2020 version of *L-Galaxies* that was adapted from Fu et al. (2013) is the introduction of concentric annuli. By default, the model features twelve such annuli that are logarithmically-spaced and act as the resolution limit for the cold gas and stars within a galaxy’s disk and stars within a galaxy’s bulge. The annuli’s outer radii have values of

$$w_j / [h^{-1} \text{kpc}] = 0.01 \times 2^j \quad \text{with } j \in [1, 12], \quad (1)$$

resulting in  $w_1 \approx 29.7 \text{ pc}$  and  $w_{12} \approx 60.8 \text{ kpc}$ .

One of the affected properties of the separation into annuli is the star formation prescription. *L-Galaxies* assumes that the molecular gas in each annulus collapses on a dynamical time-scale  $\tau_{\text{dyn}}$  and is transformed to stars with an efficiency  $\epsilon_{\text{H}_2}$  (e.g. Fu et al. 2012). Thus, in terms of surface mass density, the SFR for ring  $j$  is

$$\Sigma_{\text{SFR}, j} = \epsilon_{\text{H}_2} \tau_{\text{dyn}}^{-1} \Sigma_{\text{H}_2, j}. \quad (2)$$

The model assumes for the dynamical time

$$\tau_{\text{dyn}} = R_g / v_{\text{max}}, \quad (3)$$

where we introduced the disk scale-length of the cold gas and the maximum value of the rotation velocity of the dark matter halo. The amount of molecular gas itself is derived from the available cold gas in each ring and, in turn, is related to the gas’ metallicity and clumping of gas clouds. Extensive discussions and recipes for computing the molecular mass (per annuli) are presented in Krumholz et al. (2009); Fu et al. (2010); McKee & Krumholz (2010); Fu et al. (2013); Henriques et al. (2020).

In this work we adopt the 2014 cosmology of *Planck* (Planck Collaboration 2014) with  $\Omega_{\Lambda, 0} = 0.685$ ,  $\Omega_{\text{M}, 0} = 0.315$  (with  $\Omega_{\text{B}, 0} = 0.0487$ ),  $\sigma_8 = 0.826$ ,  $n_s = 0.96$ , and  $h = 0.673$  throughout the paper. *L-Galaxies* itself utilises dark matter-only simulations that are re-scaled (Angulo & White 2010; Angulo & Hilbert 2015) to these cosmological parameters.

## 2.2. Gravitational potential

The computation of the fraction of star formation that is bound in star clusters (Section 2.3.3) requires knowledge of the underlying gravitational potential. We consider the contributions of all available galaxy components that *L-Galaxies* considers during the simulation, namely a central massive black hole, dark matter, a bulge, gaseous and stellar disks, and gaseous and stellar halos.

**Massive black hole** In case a massive black hole occupies a galaxy centre, we introduce a gravitational potential of a point mass, i.e.

$$\Phi_{\text{BH}}(w) = -\frac{G M_{\text{BH}}}{w}, \quad (4)$$

where  $G$  is the gravitational constant,  $M_{\text{BH}}$  the black hole mass, and  $w$  the galactocentric distance. We assume here that the galaxy centre remains in the dark matter halo’s centre at all times and that the massive black hole does

not ‘wander’ within the galaxy (see [Izquierdo-Villalba et al. 2020](#); [Untzaga et al. 2024](#), for a discussion on wandering black holes in *L-Galaxies*).

**Dark matter halo** We select a classical NFW profile ([Navarro et al. 1996](#)) to describe the distribution of dark matter. The gravitational potential is given by

$$\Phi_{\text{DM}}(w) = -\frac{G M_{\text{vir}}}{w} \frac{\ln(1 + c_{\text{vir}} w/R_{\text{vir}})}{\ln(1 + c_{\text{vir}}) - c_{\text{vir}}/(1 + c_{\text{vir}})}, \quad (5)$$

where we introduced the virial mass  $M_{\text{vir}}$  and radius  $R_{\text{vir}}$ , respectively. For the concentration parameter,  $c_{\text{vir}}$ , which relates the profile’s scale-radius to  $R_{\text{vir}}$ , we assume a relation from [Dutton & Macció \(2014\)](#) that connects it to  $M_{\text{vir}}$  via

$$\log_{10} c_{\text{vir}} = \alpha(z) + \beta(z) \times \log_{10}(M_{\text{vir}} / [10^{12} h^{-1} M_{\odot}]). \quad (6)$$

The redshift-dependent coefficients  $\alpha(z)$  and  $\beta(z)$  take values according to Table 3 of [Dutton & Macció \(2014\)](#) with  $\alpha(0) = 1.025$  and  $\beta(0) = -0.097$ .

**Galactic bulge** We model a galaxy’s bulge with a [Jaffe \(1983\)](#) profile of the form

$$\Phi_{\text{B}}(w) = -\frac{G M_{\text{B}}}{w_{\text{B}}} \ln(1 + w_{\text{B}}/w), \quad (7)$$

with a scale-length  $w_{\text{B}}$  that encloses half of the bulge’s mass  $M_{\text{B}}$ .

**Gaseous and stellar disks** We follow the default assumption in *L-Galaxies* that both the gaseous and stellar disks are well described by two-dimensional exponential density profiles. The mid-plane gravitational potential of the two disks is expressed with modified Bessel functions of the first and second kind,  $I_{\nu}$  and  $K_{\nu}$ , respectively (e.g. [Watson 1944](#); [Kuijken & Gilmore 1989](#)). The gravitational potential for disk  $i$  reads

$$\Phi_{\text{D},i}(w) = -\pi G \Sigma_{\text{D},i} w [I_0(y_i) K_1(y_i) - I_1(y_i) K_0(y_i)], \quad (8)$$

where  $y_i = w/(2 \times w_{\text{D},i})$ ,  $w_{\text{D},i}$  a characteristic scale-length, and  $\Sigma_{\text{D},i}$  as the central surface mass density ([Freeman 1970](#); [Binney & Tremaine 2008](#)).

**Hot gas and stellar haloes** We assume that a galaxy’s halo contains both hot gas that is unable to form stars and a stellar medium that originates entirely from stripped satellite galaxies. For simplicity, we assume that an isothermal profile can describe well both the gaseous and stellar halo, i.e.

$$\Phi_{\text{H},i}(w) \propto -\frac{G M_{\text{H},i}}{R_{\text{H},i}} \ln(w). \quad (9)$$

Furthermore, we assume that all mass is enclosed within the virial radius such that  $R_{\text{H},i} = R_{\text{vir}}$ .<sup>1</sup>

<sup>1</sup> [Yates et al. \(2017, 2024\)](#) discuss and utilise more physically motivated profiles within *L-Galaxies*.

### 2.3. Star cluster formation

The total mass of newly formed stars that are bound in star clusters equals the SFR multiplied by the simulation time step and the cluster formation efficiency ([Bastian 2008](#)). In principle, the latter must be computed considering local conditions of the gas phase, mergers from substructures, and accretion of gas during cluster formation (see e.g. [Karam & Sills 2022, 2023](#)) but this is not feasible with our approach.

Here we follow the prescription outlined by [Kruijssen \(2012\)](#) to estimate the cluster formation efficiency. The model relies on three quantities: (1) the cold gas surface mass density  $\Sigma_{\text{g}}$ , which we compute as an annuli’s molecular mass divided by it’s area, (2) the epicyclic frequency  $\kappa$ , and (3) the Toomre disk stability parameter  $Q$ . We compute these values for the logarithmic mean galactocentric distance of each annuli  $j$ , unless stated otherwise, and assume that it is applicable to a wide range of environments and redshifts.<sup>2</sup> Furthermore, we assume that all star clusters form in galaxy disks, thus, neglecting cluster formation during galaxy mergers or outside of dark matter halos at high- $z$  ([Lake et al. 2021, 2023](#)).

#### 2.3.1. Epicyclic frequency

Based on the combined gravitational potential of all previously introduced galaxy components,  $\Phi_{\text{tot}}(w) = \sum_c \Phi_c(w)$ , we can easily determine the epicyclic frequency for circular orbits. For annulus  $j$  and log-mean distance  $\langle w_j \rangle$ ,

$$\kappa_j = \sqrt{\frac{3}{\langle w_j \rangle} \left. \frac{\partial \Phi_{\text{tot}}}{\partial w} \right|_{\langle w_j \rangle} + \left. \frac{\partial^2 \Phi_{\text{tot}}}{\partial w^2} \right|_{\langle w_j \rangle}}. \quad (10)$$

Note that, when evaluating this property for galaxy disks, we assume co-rotation of the gaseous and stellar disks resulting in only a single value of these quantities per annuli.

#### 2.3.2. Toomre stability parameter

The Toomre stability criterion ([Safronov 1960](#); [Toomre 1964](#)) evaluates whether a disk is stable against collapse considering gravity, pressure, and shear. For the gaseous and stellar disks we determine

$$Q_{\text{g},j} = \frac{\kappa_j \sigma_{\text{D},\text{g},j}}{\pi G \Sigma_{\text{g},j}}, \quad (11a)$$

$$Q_{\text{D},j} = \frac{\kappa_j \sigma_{\text{D},\text{s},j}}{3.36 G \Sigma_{\text{s},j}}, \quad (11b)$$

where  $Q > 1$  for a stable disk. Here we introduced for the gaseous and stellar disks, respectively, the surface densities ( $\Sigma_{\text{g}} / \Sigma_{\text{s}}$ ) and the velocity dispersions ( $\sigma_{\text{D},\text{g}} / \sigma_{\text{D},\text{s}}$ ).

We follow [Bottema \(1993\)](#), but see also [van der Kruit & Freeman 2011](#)) to calculate the velocity dispersion of the stars<sup>3</sup> as

$$\sigma_{\text{D},\text{s},j} = \frac{v_{c,j}}{2} \exp\left(-\frac{\langle w_j \rangle}{2w_{\text{D}}}\right), \quad (12)$$

<sup>2</sup> Using the same cluster formation efficiency calculations from [Kruijssen \(2012\)](#), [Pfeffer et al. \(2024a\)](#) recently showed that the *E-MOSAICS* simulation can well reproduce observed properties of star clusters at high- $z$ .

<sup>3</sup> Here we completely neglect the increase in velocity dispersion as a function of stellar age caused by interactions with giant molecular clouds or spiral waves, potentially resulting in a more stable disk.

with circular velocity

$$v_{c,j} = \sqrt{\langle w_j \rangle \frac{\partial \Phi_{\text{tot}}}{\partial w} \Big|_{\langle w_j \rangle}}. \quad (13)$$

We assume that the velocity dispersion of the cold gas equals the speed of sound of the interstellar medium, which correlates with the star formation surface density, i.e.

$$c_{s,\text{cold},j} = \alpha_{\text{cold}} + \beta_{\text{cold}} \times \left( \frac{\Sigma_{\text{SFR},j}}{[\text{M}_{\odot} \text{ kpc}^{-2} \text{ yr}^{-1}]} \right)^{\gamma_{\text{cold}}}, \quad (14)$$

with free parameters  $\alpha_{\text{cold}}$ ,  $\beta_{\text{cold}}$ , and  $\gamma_{\text{cold}}$ . This relationship shows significant scatter in observations across various redshifts (see e.g. [Lehnert et al. 2009](#); [Genzel et al. 2011](#); [Green et al. 2014](#); [Krumholz & Burkhardt 2016](#); [Zhou et al. 2017](#); [Krumholz et al. 2018](#); [Mai et al. 2024](#), and references therein). In our fiducial model we assume the parameter values  $\alpha_{\text{cold}} = 5 \text{ km s}^{-1}$ ,  $\beta_{\text{cold}} = 20 \text{ km s}^{-1}$ , and  $\gamma_{\text{cold}} = 1/3$ , i.e. a turbulence-dominated energy dissipation prescription for the cold gas ([Zhou et al. 2017](#)). We explore the impact of different values in [Appendix A.1](#).

It is well known that the gaseous and stellar disks interact dynamically (e.g. [Lin & Shu 1966](#); [Bertin & Romeo 1988](#)) and that, for example, the stability of a stellar disk may be impacted by even small amounts of gas. To retain the same guidelines for the Toomre stability parameter in the prescription provided by [Kruijssen \(2012\)](#) we follow the approach by [Romeo & Wiegert \(2011\)](#) and compute an ‘‘effective’’ Toomre parameter as

$$Q_{\text{eff},j}^{-1} = \begin{cases} \psi_{Q,j} Q_{s,j}^{-1} + Q_{g,j}^{-1} & \text{if } Q_{s,j} \geq Q_{g,j}, \\ Q_{s,j}^{-1} + \psi_{Q,j} Q_{g,j}^{-1} & \text{otherwise,} \end{cases} \quad (15)$$

with the weighting factor

$$\psi_{Q,j} = 2 \frac{\sigma_{\text{D},s,j} \times \sigma_{\text{D},g,j}}{\sigma_{\text{D},s,j}^2 + \sigma_{\text{D},g,j}^2}. \quad (16)$$

We show in [Figure 2](#) an overview of the cold gas surface mass density, the epicyclic frequency, and the Toomre stability parameter for disk- and bulge-dominated galaxies from running our model on tree-files of the Millennium simulation. For comparison, we add the position of the solar neighbourhood.

The epicyclic frequency and cold gas surface density decrease at larger galactocentric distances. The Toomre parameter shows a more complex behaviour, typically ranging between one and ten, except for the largest distances, where it sharply increases for most galaxies and the centre of ellipticals, where it increases as well. The latter effect is caused by the importance of the bulge component, which is weaker in spirals. At large radii the disks of low-mass galaxies are barely populated with gas and stars, which drive  $Q_{\text{eff}}$  to large values. For the same reason the Toomre parameter drops for more massive galaxies, which is reflected by an increase in the disk’s scale-length. Overall we find good agreement between our simulated galaxies and the solar neighbourhood.

### 2.3.3. Bound fraction of star formation

The bound fraction of newly formed stars in star clusters is closely related to the cluster formation efficiency ([Bastian](#)

[2008](#); [Goddard et al. 2010](#); [Adamo et al. 2011](#); [Silva-Villa & Larsen 2011](#)), which takes into account its survival rate during the first few Myr. Although important in many aspects, it is unclear how the bound fraction and cluster formation efficiency are related to the interstellar medium and star formation (see [Andersson et al. 2024](#), for a recent discussion on how feedback influences the cluster formation efficiency).

As mentioned above, we follow the model outlined by [Kruijssen \(2012\)](#) to estimate the bound fraction based on its epicyclic frequency, cold gas surface density, and Toomre stability parameter, all equated at the log-mean galactocentric distance. We briefly highlight key aspects of the model and refer the interested reader to the original work for a more detailed description.

Note that we do not directly determine the bound fraction during the execution of the simulation. Instead, to reduce the computational cost, we create lookup tables for a set of  $\{\Sigma_{\text{g}}, Q_{\text{eff}}, \kappa\}$ . In total, we utilise 18 lookup tables with varying values of  $Q_{\text{eff}}$  (between 0.01 and 4.0) and 500 values of  $\Sigma_{\text{g}}$  and  $\kappa$  each, resulting in  $4.5 \times 10^6$  data points. The simulation then determines the closest match in all three parameters and extracts the bound fraction from the table.

Following an extensive literature (e.g. [Padoan et al. 1997](#); [Vázquez-Semadeni et al. 1998](#); [Ostriker et al. 2001](#); [Kritsuk et al. 2007](#); [Padoan & Nordlund 2011](#); [Kritsuk et al. 2017](#); [Burkhart 2018](#)) we assume that the density contrast of the interstellar medium follows a log-normal distribution of the form

$$dp_j = \frac{1}{\sqrt{2\pi}\varsigma_{\rho,j}} \exp\left[-\left(\frac{\ln \delta_j - \overline{\ln \delta_j}}{\sqrt{2}\varsigma_{\rho,j}}\right)^2\right] d(\ln \delta_j), \quad (17)$$

with relative density  $\delta_j = \rho/\rho_{\text{ISM},j}$ ,  $\overline{\ln \delta_j} = -0.5\varsigma_{\rho,j}^2$  (e.g. [Vázquez-Semadeni 1994](#)), and standard deviation

$$\varsigma_{\rho,j} = \sqrt{\ln(1 + 3\gamma_{\rho}^2 \mathcal{M}_{\text{cold},j}^2)}, \quad (18)$$

where  $\gamma_{\rho} \approx 0.5$  ([Nordlund & Padoan 1999](#); [Padoan & Nordlund 2002](#)). We determine the density of the interstellar medium as

$$\rho_{\text{ISM},j} = \frac{\phi_{\text{P}}}{2\pi\text{G}} \left( \frac{\kappa_j}{Q_{\text{eff},j}} \right)^2, \quad (19)$$

with  $\phi_{\text{P}} \approx 3$  (see [Appendix A](#) of [Krumholz & McKee 2005](#)). The Mach number of the cold gas is related to the cold gas surface density, the epicyclic frequency, and the Toomre stability parameter via

$$\mathcal{M}_{\text{cold},j} = \sqrt{2} \phi_{\overline{\text{P}},j}^{1/8} \frac{Q_{\text{eff},j} \Sigma_{\text{g},j}}{\kappa_j}, \quad (20)$$

where  $\phi_{\overline{\text{P}},j}$  is the ratio of the mean pressure of a gaseous cloud related to the pressure at its surface ([Krumholz & McKee 2005](#)) with typical values close to two in dense regions ([Heyer et al. 2004](#); [Rosolowsky & Blitz 2005](#); [Schuster et al. 2007](#); [Colombo et al. 2014](#)). Notice that the parameter  $\phi_{\overline{\text{P}},j}$  is directly related to the fraction of cold gas contained in giant molecular clouds (GMCs) as  $\phi_{\overline{\text{P}},j} \approx 10 - 8 \times f_{\text{GMC},j}$ . We assume that this fraction only depends on the cold gas surface density ([Krumholz & McKee 2005](#)), i.e.

$$f_{\text{GMC},j} = \left[ 1 + 250 / (\Sigma_{\text{g},j} / [\text{M}_{\odot} \text{ pc}^{-2}])^2 \right]^{-1}. \quad (21)$$

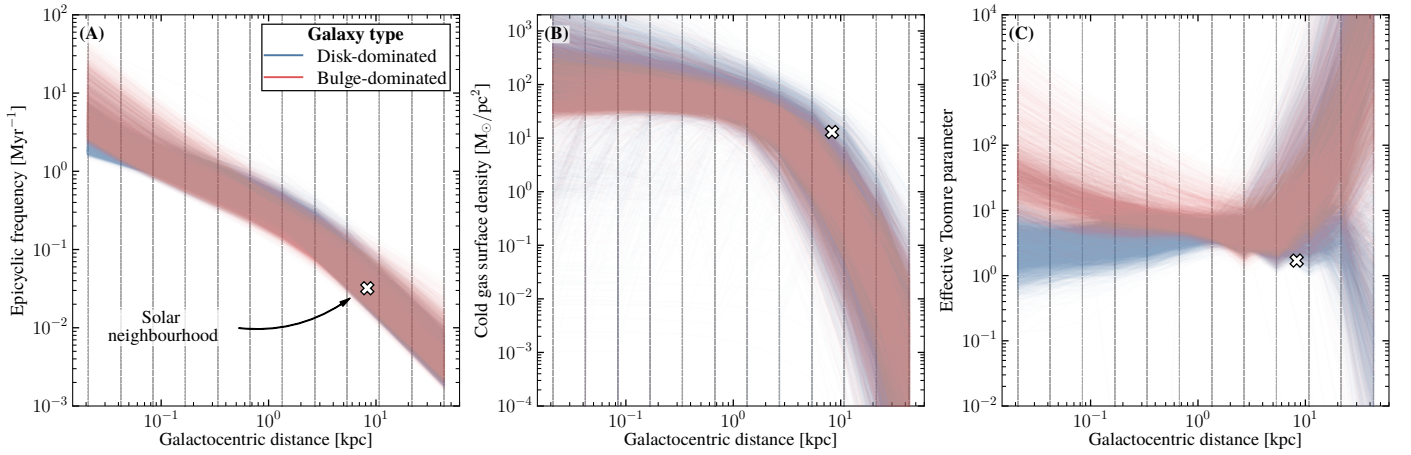


Fig. 2: Epicyclic frequency, cold gas surface mass density, and the Toomre stability parameter as a function of galactocentric distance for disk- (blue) and bulge-dominated (red) galaxies, defined as having a bulge-to-total stellar mass ratio of  $B/T < 0.2$  and  $B/T \geq 0.9$ , respectively. We add for comparison the value of the solar neighbourhood: we calculate  $\kappa_{D,\odot} \approx 0.046 \text{ Myr}^{-1}$ , as derived from the Oort constants  $A = 15.6 \text{ km s}^{-1} \text{ kpc}^{-1}$  and  $B = -15.8 \text{ km s}^{-1} \text{ kpc}^{-1}$  taken from Guo & Qi (2023);  $\Sigma_{g,\odot} \approx 13 M_{\odot} \text{ pc}^{-2}$  from Flynn et al. (2006); and  $Q_{\text{eff},\odot} \approx 1.7$  (Binney & Tremaine 2008, with  $Q_{s,\odot} \approx 2.7$  and  $Q_{g,\odot} \approx 1.5$ ), a typical value for disks (e.g. Rafikov 2001; Leroy et al. 2008; Feng et al. 2014; Westfall et al. 2014).

Next, we need to evaluate the minimum-value star formation efficiency. If star formation occurs on the free-fall time scale, this efficiency can be expressed as a combination of the specific SFR,  $\text{sSFR}_{\text{ff}}$ , and the ratio of the feedback time scale,  $t_{\text{fb}}$ , to the free-fall time scale,  $t_{\text{ff}}$ , i.e.

$$\epsilon_{\text{ff},j} = \text{sSFR}_{\text{ff},j} \times t_{\text{fb},j} / t_{\text{ff},j}. \quad (22)$$

For a spherical symmetric and homogeneous mass distribution,

$$t_{\text{ff},j} = \sqrt{\frac{3\pi}{32G \rho_{\text{ISM},j}}}. \quad (23)$$

For the feedback time scale (Kruijssen 2012),

$$t_{\text{fb},j} = \frac{t_{\text{SN}}}{2} \left[ 1 + \sqrt{1 + \frac{4\pi^2 G^2 t_{\text{ff},j}}{\phi_{\text{fb}} \text{sSFR}_{\text{ff},j} t_{\text{SN}}^2} \times \left( \frac{Q_{\text{eff},j} \Sigma_{g,j}}{\kappa_j} \right)^2} \right], \quad (24)$$

where  $t_{\text{SN}}$  is the time scale for the first supernovae, which we assume to be 3 Myr,  $\phi_{\text{fb}} = 5.28 \times 10^2 \text{ pc}^2 \text{ Myr}^{-3}$  (Kruijssen 2012), and

$$\frac{\text{sSFR}_{\text{ff},j}}{0.13} = 1 + \text{erf} \left[ \frac{\zeta_{\rho,j}^2 - \ln(0.68 \alpha_{\text{vir}}^2 \mathcal{M}_{\text{cold},j}^4)}{2^{3/2} \zeta_{\rho,j}} \right], \quad (25)$$

with the virial parameter of GMCs  $\alpha_{\text{vir}}$  (Larson 1981). It relates the mass, size, and velocity dispersion of a GMC and takes values between  $10^{-1}$  and  $10^1$  (e.g. Myers & Goodman 1988; Bertoldi & McKee 1992; Heyer et al. 2009; Dobbs et al. 2011; Hopkins et al. 2012). We set  $\alpha_{\text{vir}} = 1.3$  as proposed by McKee & Tan (2003).

In case star formation is less efficient than is assumed in Equation 22 we take  $\epsilon_{\text{inc},j} = \epsilon_{\text{ff},j} \times t_{\text{fb},j} / 10 \text{ Myr}$ . If star formation is more efficient we set an upper bound of  $\epsilon_{\text{inc},j} = \epsilon_{\text{max}} = 0.5$  (Matzner & McKee 2000). The resulting effective star formation efficiency is the minimum of the above values,

$$\epsilon_j = \min(\epsilon_{\text{ff},j}, \epsilon_{\text{inc},j}, \epsilon_{\text{max}}). \quad (26)$$

Finally, the bound fraction of star formation can be computed by the normalised integral of the probability density function of contrast of the interstellar medium combined with the minimum star formation efficiency,

$$f_{\text{bound},j} = \epsilon_{\text{max}}^{-1} \frac{\int_{-\infty}^{\infty} d\delta_j \epsilon_j^2(\delta_j) \delta_j (dp_j/d\delta_j)}{\int_{-\infty}^{\infty} d\delta_j \epsilon_j(\delta_j) \delta_j (dp_j/d\delta_j)}. \quad (27)$$

Figure 3 shows the bound fraction for different environments with  $Q_{\text{eff}} = 0.5$  for the background. The  $z = 0$  distribution of annuli from running *L-Galaxies* on halos identified in the Millennium and Millennium-II simulations that satisfy  $Q_{\text{eff}} < 2$  is added on top and reveals a large range bound star formation that depends on the location within the galaxy: the innermost regions feature high surface densities and epicyclic frequencies (*c.f.* Figure 2) and have high bound fractions approaching one. In contrast, the outermost regions of galaxies have low surface densities and epicyclic frequencies, prohibiting the formation of bound structures. As a consequence, this result already predicts that massive star clusters at distances a few times the disk's scale-length likely originate from accreted satellite galaxies, assuming that heating processes within their host galaxy are insignificant.

While not shown in Figure 3, we find a decrease in bound fraction for an increasing Toomre stability parameter value when keeping the epicyclic frequency and cold gas surface density constant. This is related to the specific SFR,  $\text{sSFR}_{\text{ff}}$ , which decreases for an increasing Toomre parameter as per Equations 20 and 25, and because the gas disk becomes more stable with an increase in  $Q_{\text{eff}}$ . As a result the mid-plane density of the interstellar medium decreases, which, in turn, decreases the star formation efficiency and, thus, the bound fraction.

#### 2.4. Initial star cluster properties

Here we detail the initial properties of star clusters that form in galaxy disks. Note that we deliberately exclude star clusters that form in the innermost ring with a radius

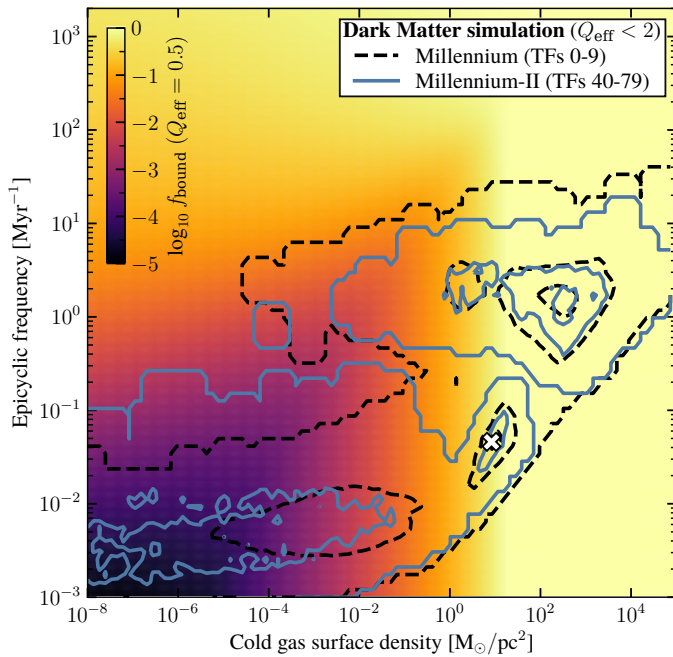


Fig. 3: Bound fraction of star formation, evaluated for  $Q_{\text{eff}} = 0.5$ , as a function of epicyclic frequency and cold gas surface density. Blue solid and dashed black contours give the smoothed distribution (with standard deviation of 1 dex) of all annuli of all galaxies with  $Q_{\text{eff}} < 2$  after running *L-Galaxies* tree-files 0-9 and 40-79 on the Millennium and Millennium-II simulations, respectively. Contour lines are smoothed with a Gaussian kernel with standard deviation of 0.5 dex. The location of the solar neighbourhood (see Figure 2 for details) is marked with a white cross.

of approximately 30 pc. These star clusters will either be disrupted quickly or merge to form a nuclear star cluster, which will be the subject of future work.

Another computational limit is the number of star clusters whose properties will be tracked over time. In this work, we focus on the most massive star clusters that survive until  $z = 0$  and decide to completely ignore star clusters below  $10^3 M_{\odot}$  (see below). In the simulation we track the properties of the 1000 most massive star clusters in the disk and halo, respectively, resulting in up to 2000 objects per galaxy. Although somewhat arbitrary, these numbers compare to the total number of star clusters of M31 (potentially more than 1000; e.g. Barmby & Huchra 2001; Huxor et al. 2014) and is much larger than the number of known globular clusters for the Milky Way (about 200; see e.g. Minniti et al. 2017; Garro et al. 2024, and references therein). In case a galaxy forms less than 1000 massive star clusters above throughout its life time, all other masses are ignored and not considered in the below analysis.

#### 2.4.1. Stellar mass

The mass of each star cluster is a random realisation of the underlying cluster initial mass function (CIMF), which we assume to follow a classical power-law function that is truncated at the upper mass end with an environmentally-dependent mass-scale, i.e.

$$\xi_j(m_c) \propto m_c^{\alpha_{\text{CIMF}}} \times \exp(-m_c / m_{\text{cl,max},j}). \quad (28)$$

We assume here that  $\alpha_{\text{CIMF}} = -2$ , motivated by observational studies of young star clusters in nearby galaxies (e.g. Zhang & Fall 1999; Bik et al. 2003; Hunter et al. 2003; McCrady & Graham 2007; Portegies Zwart et al. 2010; Emig et al. 2020; Levy et al. 2024). The truncation mass-scale is a product of the star formation efficiency ( $\epsilon_{\text{cloud}}$ ), the bound fraction of star formation ( $f_{\text{bound}}$ ), the Toomre mass ( $m_{\text{T}}$ ), and the fraction of molecular gas that is critical to undergo gravitational collapse ( $f_{\text{coll}}$ ; Reina-Campos & Kruijssen 2017, but see also Kruijssen 2014 and Reina-Campos et al. 2022a), i.e.

$$m_{\text{cl,max},j} = \epsilon_{\text{cloud}} \times f_{\text{bound},j} \times m_{\text{T},j} \times f_{\text{coll},j}, \quad (29)$$

resulting in a typical value of the order of  $10^5 M_{\odot}$  at lower redshifts and up to  $10^9 M_{\odot}$  in extreme cases. We assume

$$m_{\text{T},j} = 4\pi^5 G^2 \times \Sigma_{\text{g},j}^3 \times Q_{\text{eff},j}^4 / \kappa_j^4, \quad (30)$$

and

$$f_{\text{coll},j} = \min(1, t_{\text{fb},j} / t_{\text{ff,2D},j})^4, \quad (31)$$

for the Toomre mass and collapse fraction, respectively. The two-dimensional free-fall time scale is  $t_{\text{ff,2D},j} = \sqrt{2\pi} / \kappa_j$ .

In the above equations we assume a constant value of  $\epsilon_{\text{cloud}} = 0.1$  for star formation within a GMC, motivated by numerical results (e.g. Oklopčić et al. 2017; Chevance et al. 2020). Notice that this value is potentially smaller than the assumed star formation efficiency in the determination of the bound fraction in Equation 26. A higher efficiency would result in a higher upper truncation mass-scale of the CIMF and could result in the formation of more massive star clusters. However, as we show in Appendix A.3 the main results of our work do not significantly change when assuming no upper truncation mass-scale but a pure power-law function instead.

For computational efficiency of the code, we consider only star clusters with initial masses in the range of  $10^4$  to  $10^8 M_{\odot}$ . At the same time, we assume that the minimum star cluster mass that could, in principle, form is  $10^2 M_{\odot}$ , meaning that we do not fully sample the CIMF. Therefore, we only sample a total star cluster mass of  $f_{\text{sample}} \times f_{\text{bound}} \times \text{SFR} \times \delta t$  where

$$f_{\text{sample}} = \frac{\int_{10^4 M_{\odot}}^{10^8 M_{\odot}} m_c \xi(m_c) dm_c}{\int_{10^2 M_{\odot}}^{10^8 M_{\odot}} m_c \xi(m_c) dm_c}. \quad (32)$$

In the case of a power-law CIMF with index  $-2$  this ratio is two-thirds, i.e. one-third of the total mass in star clusters is contained in objects below  $10^4 M_{\odot}$ . For the more complex case of Equation 28, we pre-compute the integral numerically for seven equally-spaced values between  $10^3$  and  $10^9 M_{\odot}$ , resulting in, for example,  $f_{\text{sample}} \approx 2.3 \times 10^{-6}$  for  $m_{\text{cl,max}} = 10^3 M_{\odot}$ . Afterwards, we randomly sample the CIMF with  $m_{\text{cl,max}}$  that agrees best with the computed value of Equation 29.

Finally, to reduce computational cost we utilise lookup tables for initial star cluster masses. For simplicity, we generated seven lookup tables for different values of  $m_{\text{cl,max}}$ , equally spaced between  $10^3$  and  $10^9 M_{\odot}$ , with  $10^5$  data points each. Randomly sampling data points from the lookup tables turned out to be computationally more efficient than direct random sampling from the cluster initial mass functions as many of the drawn star cluster masses are too low to be stored in arrays.

### 2.4.2. Initial galactocentric distances

For each annulus we assume that the galactocentric distribution of initial values is uniform and independent of other star cluster parameters.

### 2.4.3. Half-mass radius

The physical processes that govern the distribution of the initial half-mass radius of star clusters is still unknown, and many theoretically motivated and observational-based prescriptions seem to fail to reproduce the distribution at  $z = 0$  in nearby galaxies (e.g. [Reina-Campos et al. 2023a](#)). For that reason we adopt a simplified prescription by using a constant initial value of  $r_{c,h} = 1.0$  pc for all clusters, independent of mass and redshift of formation. We explore more complex prescriptions in Appendix A.2.

### 2.4.4. Tidal radius

The half-mass sizes of star clusters increase over time (*c.f.* Section 2.5.2) and are limited to the tidal radius where the gravitational acceleration of the cluster equals the tidal acceleration. The tidal field is directly related to the local gravitational potential and the tidal radius is related to the first eigenvector of the diagonalised tidal tensor. Assuming circular orbits and a mass concentration in the galaxy centre we apply the definition of [King \(1962, but see also Renaud et al. 2011; Renaud 2018\)](#) and calculate

$$r_{c,t} = \left[ \frac{G m_c}{(\Omega^2 - \partial^2 \Phi_{\text{tot}} / \partial w^2)_{w_c}} \right]^{1/3}, \quad (33)$$

where  $\Omega$  equals the angular frequency equated at the galactocentric distance of the star cluster. More generally, for each ring  $j$ ,

$$\Omega_j = \sqrt{\left. \frac{1}{\langle w_j \rangle} \frac{\partial \Phi_{\text{tot}}}{\partial w} \right|_{\langle w_j \rangle}}. \quad (34)$$

Note that this prescription ignores the tidal effect of nearby baryonic over-densities, such as star forming regions or clouds, which may be dominant over the global galactic field. Other works that use hydrodynamical approaches (such as [Reina-Campos et al. 2022a](#)) determine a local tidal tensor from neighbouring cells, which is not possible in our model. We discuss this issue in Section 3.5.

### 2.4.5. Metallicity

For the metallicity (and individual elemental abundances of H, He, C, N, O, Ne, Mg, Si, S, Ca, Fe) of a star cluster we assume that it equals the metallicity of the cold gas in the ring it forms in,  $Z_c = Z_g$ , and that this value remains constant over the star cluster’s lifetime. The first assumption neglects any azimuthal variations of metallicity profiles which are known to exist in some galaxies due to asymmetric structures such as bars or spiral patterns in the Milky Way (e.g. [Poggio et al. 2022; Spina et al. 2022; Filion et al. 2023; Hawkins 2023; Hackshaw et al. 2024](#)) and other spiral galaxies (e.g. [Sánchez-Menguiano et al. 2016; Ho et al. 2017; Sánchez-Menguiano et al. 2018; Ho et al. 2019; Hwang et al. 2019; Metha et al. 2021, 2024](#)) but see [Kreckel et al. \(2019\)](#) for counterexamples. Nevertheless, despite lacking such an

implementation we argue in Section 3.4 that the metallicity distributions of our cluster populations are reasonable.

## 2.5. Star cluster evolution

We detail in the next subsections the main processes that affect the evolution of star clusters: mass loss rates, expansion of the half-mass radius, and re-location.

### 2.5.1. Mass-loss

We consider three mechanisms for cluster mass-loss: stellar evolution, tidal stripping due to an expanding cluster, and tidal shocks from interactions with GMCs, i.e.

$$\frac{dm_c}{dt} = \left. \frac{dm_c}{dt} \right|_{\text{ev}} + \left. \frac{dm_c}{dt} \right|_{\text{rlx}} + \left. \frac{dm_c}{dt} \right|_{\text{sh}}. \quad (35)$$

**Stellar evolution** To take into account cluster mass-loss from stellar evolution we assume that cluster members represent a random realisation of a single stellar population assuming a Chabrier IMF ([Chabrier 2003](#)), resulting in varying expected lifetimes. Then, for an individual  $10^5 M_\odot$  star cluster we utilise the “Stochastically Lighting Up Galaxies” library ([da Silva et al. 2012, 2014; Krumholz et al. 2015](#)) with non-rotating “Geneva” 2013 stellar tracks ([Schaller et al. 1992; Meynet et al. 1994; Ekström et al. 2012; Georgy et al. 2013](#)) and fit a linear relationship to the retained mass as a function of time. The resulting mass-loss rate at time  $t$  in [yr] is

$$\left. \frac{dm_c}{dt} \right|_{\text{ev}} = -\frac{0.13}{\ln(10)} \frac{m_c^{\text{init}}}{t}, \quad \text{for } t \geq t_{\text{SN}}. \quad (36)$$

We find that this relation holds, to first order, irrespective of cluster metallicity. Note that the above determination does not take into account other mass-loss channels that we introduce below, which is why we update the “initial” star cluster mass, denoted here with  $m_c^{\text{init}}$ , at each time-step.

**Relaxation** Multi-body encounters between stars within a cluster result in energy transfer between the individual bodies and can cause stars to either orbit the star cluster’s centre at larger radii or leave the cluster completely in case its velocity exceeds the escape velocity. For bound stars, if the new orbit crosses the tidal radius, the star can be stripped from the cluster, resulting in an effective mass loss.

We consider this effect by following an extensive literature (e.g. [Spitzer 1940; Hénon 1961; Spitzer 1987; Lamers et al. 2005](#)) and set

$$\left. \frac{dm_c}{dt} \right|_{\text{rlx}} = -\xi_{\text{rlx}} \frac{m_c}{\tau_{\text{rlx}}}, \quad (37)$$

with a relaxation time scale

$$\tau_{\text{rlx}} = 0.138 \frac{\sqrt{N}}{\ln(\gamma_{\text{rlx}} N)} \sqrt{\frac{r_{c,h}^3}{G \langle m_\star \rangle}}. \quad (38)$$

Here  $\langle m_\star \rangle$  is the average stellar mass of the star cluster,  $N = m_c / \langle m_\star \rangle$ , and  $0.07 \lesssim \gamma_{\text{rlx}} \lesssim 0.14$  ([Giersz & Heggie 1994](#)). We assume a [Chabrier \(2003\)](#) initial stellar mass function, such that  $\langle m_\star \rangle = 0.42 M_\odot$  and  $\gamma_{\text{rlx}} = 0.11$ . Finally,

we choose  $\xi_{\text{rlx}} = 0.08$  as suggested in the literature (e.g. Hénon 1961; Gieles et al. 2011; Gieles & Renaud 2016) for equal-mass cluster members, avoiding a proper treatment of the star cluster’s direct tidal environment (Alexander & Gieles 2012).

**Tidal shocks** When a star cluster is located within the thin disk, i.e. has not been accreted during a galaxy merger event, it frequently interacts with GMCs if the fraction of cold gas bound within clouds is high. Depending on the impact parameter between the interaction the GMC can inject a significant amount of energy into the star cluster resulting in an increase in velocity dispersion and causing a fraction of the stars to escape the cluster as their velocity exceeds the cluster’s escape velocity.

To model this effect we approximate a cluster’s internal energy by assuming that it follows a Plummer-like density profile (Plummer 1911). Following the equations outlined in Kruijssen (2012) we set

$$\left. \frac{dm_c}{dt} \right|_{\text{sh}} = -\frac{m_c}{\tau_{\text{sh}}}, \quad (39)$$

with

$$\tau_{\text{sh}} = \frac{3\sqrt{\pi}}{2\sqrt{2^{2/3}-1}} \frac{G}{g\phi_{\text{sh}}\phi_{\text{ad}}\phi_{\text{P}}f_{\text{sh}}} \times \left[ \frac{Q_{\text{eff},j}}{\kappa_j f_{\text{GMC}}^{1/3}} \right]_{w_c}^3 \frac{m_c}{r_{c,h}^3}, \quad (40)$$

with  $g = 1.5$ ,  $\phi_{\text{sh}} = 2.8$ ,  $f_{\text{sh}} = 3$  and  $\phi_{\text{ad}} = \exp(-0.062)$ . We use Equation 21 to equate  $f_{\text{GMC}}$  for the annuli corresponding to the star cluster’s current galactocentric distance.

Note that, as mentioned above, only star clusters in galaxy disks are affected by tidal shocks due to encounters with GMCs, i.e. we set  $dm_c/dt|_{\text{sh}} = 0$  for star clusters in a galaxy’s halo. Our implementation also does not couple the time scale of tidal shocks to the strength of the local tidal field tensor (see e.g. Alexander et al. 2014; Reina-Campos et al. 2022a, for details) because we do not attempt to model GMCs. However, because *L-Galaxies* already separates the atomic from the molecular gas in each annulus (see Henriques et al. 2020; Yates et al. 2021, but also Yates et al. 2024) future efforts may implement clouds and improve on the current prescription.

### 2.5.2. Radial expansion

Star clusters expand adiabatically due to contributions from mass-loss from two-body interactions and tidal shocks (e.g. Reina-Campos et al. 2022a). This results in a radial expansion of the form

$$\frac{dr_{c,h}}{dt} = \left[ (2 - f_{\text{sh}}^{-1}) \left. \frac{dm_c}{dt} \right|_{\text{sh}} + (2 + \zeta_{\text{rlx}}^{-1}) \left. \frac{dm_c}{dt} \right|_{\text{rlx}} \right] \frac{r_{c,h}}{m_c}, \quad (41)$$

Following Gieles & Renaud (2016) we assume that  $f_{\text{sh}} = 3$  and following Gieles et al. (2011)

$$\zeta_{\text{rlx}}^{-1} = \frac{5}{3} \left[ \left( \frac{r_{c,h}}{r_{c,j}} \right)_1 \frac{r_{c,j}}{r_{c,h}} \right]^{3/2} \approx 0.092 \left( \frac{r_{c,t}}{r_{c,h}} \right)^{3/2}, \quad (42)$$

where we assumed in the approximation that the Jacobi radius equals the tidal radius and that  $(r_{c,h}/r_{c,j})_1 \approx 0.145$  (Hénon 1961).

Note that we neglect here any impact of stellar-mass black holes on the evolution of the cluster, which contributes and may even dominate the dissolution of some star clusters, depending on, among others, mass and metallicity (e.g. Giersz et al. 2019; Gieles et al. 2021; Rostami-Shirazi et al. 2024). We discuss this issue again in Section 3.5.

### 2.5.3. Galactocentric migration

Without any external perturbations star clusters in a galaxy’s disk and halo migrate towards the inner regions through dynamical friction caused by interactions with constituents of three components: (1) field stars belonging to the stellar halo and bulge, (2) the gaseous halo, and (3) the dark matter halo. For the stellar and dark matter components, we follow the well-known Chandrasekhar (1943) prescription and assume an isotropic velocity distribution function of the components as well as circular orbits of the star clusters. As a consequence, a star cluster experiences a radial acceleration of

$$\frac{dv_c}{dt} = -4\pi G^2 \frac{m_c \rho_f}{v_c^2} \ln \Lambda \left[ \text{erf}(X) - \frac{2X}{\sqrt{\pi}} \exp(-X^2) \right], \quad (43)$$

where  $X = v_c / (2\sigma_f)$  and  $\rho_f$  is the density of dark matter and stars in the halo evaluated at the position of the star cluster. The circular velocity of each object is computed via Equation 13. For the Coulomb logarithm, we follow Binney & Tremaine (2008) and assume

$$\ln \Lambda = \ln \left[ \frac{w_c}{\max(r_{c,h}, G m_c / v_{\text{typ}}^2)} \right], \quad (44)$$

where we replaced the maximum impact parameter with the galactocentric distance of the star clusters and assume for the typical velocity of the stellar disk  $v_{\text{typ}} = \sqrt{G M_{\text{D},s} / R_{\text{D},s}}$ . For the velocity dispersion of halo stars we assume that their orbits are dominated by the underlying dark matter profile. Based on the Jeans equation for an isotropic system Zentner & Bullock (2003) give the following approximation for the velocity dispersion,

$$\sigma_{\text{H},s} = v_{\text{max}} \times \frac{1.4393 x_c^{0.354}}{1 + 1.1756 x_c^{0.725}}, \quad (45)$$

with maximum circular velocity within the dark matter halo that we introduced in Equation 3 and  $x_c = w_c / R_{\text{vir}}$ .

The radial acceleration caused by the hot gaseous component is slightly different compared to Equation 43. Following Ostriker (1999) and Escala et al. (2004) we take

$$\frac{dv_c}{dt} = -\frac{4\pi G^2 m_c \rho_{\text{H}}}{v_c^2} g(\mathcal{M}_{\text{hot}}), \quad (46)$$

where  $\rho_{\text{H}}$  is the density of the gaseous halo evaluated at the star clusters position and

$$g(\mathcal{M}_{\text{hot}}) = \begin{cases} \ln \Omega \times k(\mathcal{M}_{\text{hot}}) & \text{if } \mathcal{M}_{\text{hot}} < 0.8, \\ 3 \ln \Omega \times k(\mathcal{M}_{\text{hot}}) & \text{if } 0.8 \leq \mathcal{M}_{\text{hot}} \leq 1.5, \\ \ln(1 - \mathcal{M}_{\text{hot}}^{-2}) + 2 \ln \Omega & \text{otherwise.} \end{cases} \quad (47)$$

Here  $\Omega$  is the angular frequency, as introduced in Equation 34, evaluated at the position of the star cluster and  $\ln \Lambda$  the Coulomb logarithm from Equation 44. Finally,

$$k(\mathcal{M}_{\text{hot}}) = \text{erf}\left(\frac{\mathcal{M}_{\text{hot}}}{2}\right) - \sqrt{\frac{2}{\pi}} \mathcal{M}_{\text{hot}} \exp\left(-\frac{\mathcal{M}_{\text{hot}}^2}{2}\right). \quad (48)$$

We calculate the Mach number of a cluster within the hot gas halo as  $\mathcal{M}_{\text{hot}} = v_c / c_{s, \text{hot}}$  where (Tanaka & Haiman 2009; Choksi et al. 2017)

$$\frac{c_{s, \text{hot}}}{[\text{km s}^{-1}]} = 1.8 \sqrt{1+z} \left(\frac{M_{\text{vir}}}{10^7 M_{\odot}}\right)^{1/3} \left(\frac{\Omega_{M,0} h^2}{0.14}\right)^{1/6}. \quad (49)$$

### 2.5.4. Re-distribution during galaxy mergers

Explanations for the observed presence of star clusters in galaxy halos generally favour (a) interactions with massive perturbers (such as other star clusters or GMCs) that heat the object from its birth-place in a disk, (b) star cluster formation in galaxy outskirts during tidal interactions, or (c) a direct re-distribution during galaxy mergers. The lower tidal field and absence of tidal shocks may be an important ingredient in cluster survival as indicated by Baumgardt & Hilker (2018) who find that the Milky Way’s halo hosts all Galactic star clusters older than approximately five Gyr. Therefore, re-positioning of star clusters is an essential physical ingredient in simulating star cluster properties.

We consider two different scenarios based on the ratio of the baryonic masses of the two galaxies. Here we follow the prescription by *L-Galaxies* and assume that a major merger occurs if the mass ratio exceeds 0.1. In this case, we assume that the disks of both galaxies are destroyed and that all star clusters from both galaxies are contained within the halo of the successor galaxy. For minor galaxy mergers where the mass ratio is smaller than 0.1 we assume that the star cluster population of the more massive galaxy remains unaffected and that all accreted star clusters migrate into the halo of their new host.

Note that we assume here that all star clusters survive the tidal shock experienced during galaxy mergers, i.e. resulting in a “survival fraction” of unity (see Kruijssen & Cooper 2012; De Lucia et al. 2024, for a different approach). Furthermore, we do not add another mass-loss term for this scenario.

Generally speaking, the resulting baryonic distribution after galaxy mergers is sensitive to the initial conditions such as the galaxy mass ratio and their respective positions, orientations, and velocity vectors and magnitudes to each other. Therefore, when re-distributing star clusters from their old galactocentric distance,  $w_c^{\text{old}}$ , to the new galactocentric distance,  $w_c^{\text{new}}$ , we assume the following simple relationship,

$$w_c^{\text{new}} = D_{1 \leftrightarrow 2} \times \left(\frac{w_c^{\text{old}}}{D_{\text{max}}}\right)^{\alpha_w} \times \exp\left(-\frac{w_c^{\text{old}}}{D_{\text{max}}}\right). \quad (50)$$

Here we introduced two distance measures and a free parameter  $\alpha_w$  that we set to four. The first distance measure,  $D_{1 \leftrightarrow 2}$ , equals the three-dimensional separation between the two galaxy centres once the lower mass galaxy loses its dark matter halo. The other distance measure,  $D_{\text{max}}$ , equals either the largest galactocentric distance of the star cluster

population or three times the stellar disk’s scale length, i.e.

$$D_{\text{max}} = \begin{cases} \max_{i \in N_c}(w_{c,i}^{\text{old}}) & \text{if } \max_{i \in N_c}(w_{c,i}^{\text{old}}) \geq 3R_{D,s}, \\ 3R_{D,s} & \text{otherwise.} \end{cases} \quad (51)$$

## 3. Results

In this work we focus on basic properties of the star cluster populations at  $z = 0$ . In the following sections, we refer to a star cluster as young (old) if its age is  $\tau_c < 0.3$  Gyr ( $\tau_c \geq 8$  Gyr). Disk-dominated (“spiral”) galaxies are assumed to be the ones with a bulge-to-total stellar mass ratio of  $B/T < 0.2$  whereas bulge-dominated (“elliptical”) systems have  $B/T \geq 0.9$ .<sup>4</sup>

We focus our analysis on the output of running the model on Millennium (Springel et al. 2005) tree-files 0-9 (out of 512 total) that contain 118558 galaxies at  $z = 0$  and provide us with a representative sub-sample. The model performs similarly when running on Millennium-II (Boylan-Kolchin et al. 2009) tree-files 40-79 (a representative sub-sample; out of 512), going down to lower galaxy stellar masses, and we will detail a brief comparison in each subsection in case of differences.

### 3.1. $M_V$ -SFR relationship

A first test for our model is to reproduce the empirical relationship between the absolute  $V$ -band magnitude of the brightest young star cluster (local quantity within a galaxy) versus the host galaxy’s SFR (global quantity) within disk-dominated galaxies (e.g. Larsen 2002; Bastian 2008; Larsen 2010). Since this relation is not used as input for the simulation it serves as both a check of the models capabilities and a test to explore secondary correlations with other third quantities.

For the simulated data, as we store star cluster masses, we need to convert to the Johnson-Cousins  $V$ -band. We perform the conversion by using the Python version (Johnson et al. 2023) of the “Flexible Stellar Population Synthesis” code (Conroy et al. 2009, 2010; Conroy & Gunn 2010b,a) that uses as input the metallicity and age of a stellar population and yields an absolute magnitude in selected filterbands. Furthermore, for the computation, we assume that all star clusters are composed of a single stellar population that follows a Chabrier (2003) stellar initial mass function. To compare to observations we compile the data from Johnson et al. (2000); Larsen (2002); Rafelski & Zaritsky (2005); Bastian (2008); Annibali et al. (2009); Goddard et al. (2010); Adamo et al. (2011); Annibali et al. (2011); Pasquali et al. (2011); Silva-Villa & Larsen (2011); Cook et al. (2012); Ryon et al. (2014); Whitmore et al. (2014); Adamo et al. (2015); Lim & Lee (2015); Cook et al. (2023). Additionally, we use data from Maschmann et al. (2024) and Thilker et al. (2025, accepted), representing the results for PHANGS galaxies (see Lee et al. 2022, 2023, for details). For that data set specifically, we use stellar mass estimates from Emsellem et al. (2022) and SFR estimates from Sun et al. (2022). Otherwise, galaxy stellar masses are taken from the 50 Mpc catalogue provided by Ohlson et al. (2023).

We show the resulting parameter space for young massive star clusters in disk-dominated galaxies in Figure 4. Our

<sup>4</sup> *L-Galaxies* does not model any spiral-wave patterns in galaxies, which is why we prefer the term “disk-dominated” over “spiral”.

results show an increasing star cluster mass with increasing SFR, in qualitative agreement with the observations, although with a slightly steeper slope. To quantify the level of (dis-)agreement we perform a linear fit to the data sample and obtain uncertainties through 10 000 Monte Carlo iterations. The resulting slope values are  $\alpha_{\text{sim}} = -2.607^{+0.009}_{-0.009}$  for the simulated data and  $\alpha_{\text{obs}} = -2.02^{+0.09}_{-0.09}$  for the observations. This difference becomes smaller when constraining star clusters to younger ages (e.g.  $\alpha_{\text{sim}} \approx -2.457$  for  $\tau_c \leq 50$  Myr). Nevertheless, most of our star clusters are located in galaxies with SFRs of the order of  $10^{-1} M_{\odot} \text{yr}^{-1}$  and have absolute *V*-band magnitudes of  $M_V \approx -11$ , which is in excellent agreement with observations.

When running the model on Millennium-II data we find a better agreement for the lowest-mass (but still the most massive and young) star clusters towards lower galaxy SFRs, which is because of the higher mass resolution offered by the simulation. We observe that the slope values of the relationship changes: applying the same galaxy mass cut of  $10^{9.5} M_{\odot}$  results in a slope of  $\alpha_{\text{sim, mrii}} = -2.02^{+0.09}_{-0.09}$ , which is basically identical to the results of the observational data.

We identify a secondary dependence on galaxy stellar mass in panel (B) where the slope of the relationship is steeper for massive galaxies: when constraining the galaxy sample to stellar masses above  $10^{10} M_{\odot}$  the slope value decreases to  $\alpha_{\text{sim}} \approx -3.64$ .<sup>5</sup> This trend is mainly related to the upper truncation mass-scale for the CIMF, which decreases due to a decreasing Toomre mass and bound fraction. Galaxies with stellar masses below  $10^{9.5} M_{\odot}$  have comparable  $Q_{D, g}$  values to more massive galaxies but their  $Q_{D, s}$  values are larger because of their disk mass is dominated by gas and not stars and  $Q_{D, i} \propto \Sigma_{D, i}^{-1}$ . As a consequence, the slope value of these low-mass galaxies is  $\alpha_{\text{sim}} \approx -2.63$ .

For the cluster formation efficiency, which equals the bound fraction introduced in Equation 27 and the survival rate of star clusters during the initial few Myr (see Kruijssen & Cooper 2012; Kruijssen 2012, for details on this ‘‘cruel cradle effect’’), we find an increase with SFR (panel C). This is expected given the direct relationship between the SFR surface density and cold gas surface density (*c.f.* Equation 2) and because  $f_{\text{bound}}$  positively correlates with  $\Sigma_g$  (*c.f.* Figure 3). Our results are in excellent agreement with literature data.

We conclude that this relationship is sensitive to the resolution of the simulation and that taking into account biases in the mass range of the selected galaxy samples is important.

### 3.2. Half-mass radius and stellar mass

We show in Figure 5 the one-dimensional histograms of star cluster masses and half-mass radii. Here we do not distinguish between galaxy morphologies because of the similar prescriptions of star cluster formation. *L-Galaxies* assumes that star formation only occurs in galaxy disks and ellipticals will exhibit similar disk properties to disk-dominated galaxies in case cold gas is accreted (see Henriques et al. 2015, 2020, for details). Therefore, given the similar disk

properties the upper truncation mass of the CIMF and most star cluster properties remain comparable.<sup>6</sup>

For young star clusters we find an approximate power-law distribution of star cluster masses down to about  $10^4 M_{\odot}$  that equals the lowest possible mass value randomly sampled from the CIMF (see Section 2.4.1 for details). The distribution of simulated star clusters agree well to observational results of Brown & Gnedin (2021) who analysed the structural properties of young star clusters in a set of nearby galaxies from the *LEGUS* programme (Calzetti et al. 2015).<sup>7</sup> The only apparent difference exists at the high-mass end where there is a lack of massive star clusters in nearby disk-dominated galaxies, which may be both a result of simple number statistics, as massive and young star clusters above  $10^6 M_{\odot}$  are rare in our simulated data as well ( $\approx 0.5\%$ ), and because our data includes galaxies with high SFRs ( $\gtrsim 10 M_{\odot} \text{yr}^{-1}$  in some of the most massive disk-dominated systems), resulting in higher probability to form massive star clusters.

For old star clusters we find a broad distribution of masses. The shape of the distribution is partly related to the origin of the objects: clusters that were never displaced from a galaxy’s disk lost a significant amount of mass and populate the low-mass end. In contrast, accreted clusters in a galaxy halo lose mass at lower rates and, thus, retain a larger fraction of their birth mass over time resulting in the broad distribution and ‘‘peak’’-like structures at mass values of  $10^5$  to  $10^6 M_{\odot}$ . We presume that clusters with masses lower than  $10^3 M_{\odot}$  quickly dissolve and do not track their evolution, hence the sharp truncation at this mass value.

We find some slight differences based on the host galaxies morphology. The peak of the distribution at masses of approximately  $10^5 M_{\odot}$  differs by a factor of a few between disk-dominated galaxies (peak at higher-masses) and ellipticals. This difference is related to a more diverse accretion history of ellipticals resulting in a superposition of various cluster populations. Disk-dominated galaxies feature a higher fraction of massive star clusters ( $m_c \gtrsim 10^6 M_{\odot}$ ), which is due to their elevated star formation.

The distribution of half-mass radii for young star clusters is confined to small radii ranging between 1 and 5 pc. The lower bound is due to the constant half-mass radius chosen in our model, thus, the range of half-mass radii displays the environmental effect on the star clusters within the first few hundred Myr.

Our simulation fails to account for the most extended young star clusters in the sample of Brown & Gnedin (2021) that extend to  $\approx 25$  pc. At the same time, their data include a large fraction of star clusters ranging from  $\approx 0.1$  to a peak value of  $\approx 2$  pc, where the distribution of the simulated clusters peaks as well. If the data by Brown & Gnedin (2021) present a representative distribution of half-mass radii shortly after cluster birth then they indicate that the radii are potentially constrained by the clusters environment and may evolve quickly (see e.g. Banerjee & Kroupa 2017, for *N*-body simulations). Evidence for the latter comes from hydrodynamical simulations of Lahén et al. (2024b)

<sup>6</sup> There still remains some difference in the metallicities of newly formed star clusters between galaxies of different morphology, as we show in Section 3.4.

<sup>7</sup> For the comparison we applied the same age cut to the observational sample. Star cluster ages come from fitting the spectral energy distribution; see details in Adamo et al. (2017) and Ryon et al. (2017).

<sup>5</sup> Note that the secondary dependence on galaxy mass is also present in the *E-MOSAICS* model (Figure 10 in Pfeffer et al. 2019b), however, they only include 153 galaxies and have an additional *y*-axis offset of 0.5 to 1 dex.

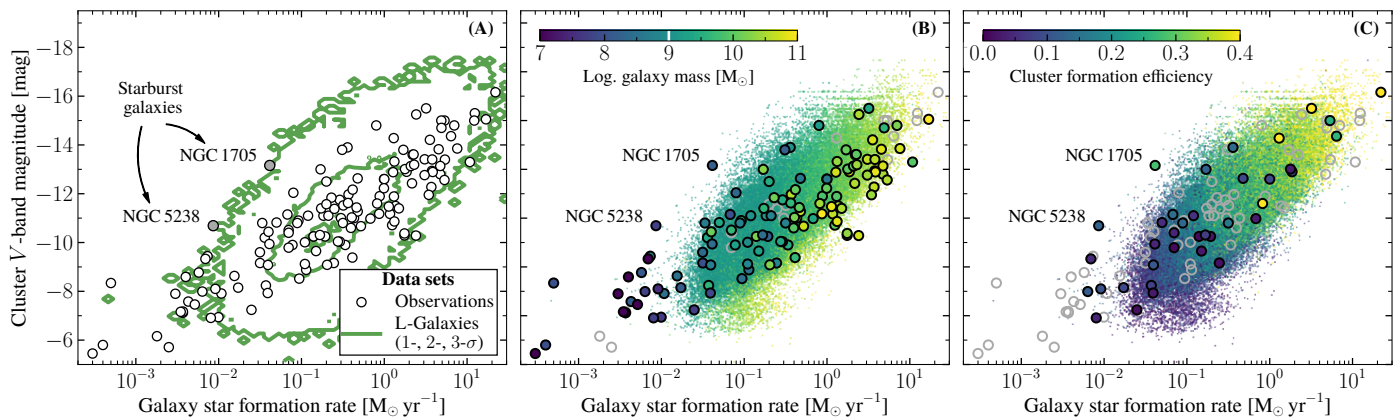
Youngest ( $\tau_c < 0.3$  Gyr) and most massive star cluster in spirals ( $B/T < 0.2$ )


Fig. 4: Absolute  $V$ -band magnitude of the youngest and most massive star cluster versus the galaxy-averaged star formation rate. The galaxy sample is limited to disk-dominated galaxies that have a bulge-to-total stellar mass ratio of  $B/T < 0.2$ . We compare our results to various observations of nearby disk-dominated galaxies (see main text for details). For both the simulated data and the observations, we set an age cut of  $\tau_c \leq 0.3$  Gyr on the star clusters. *Panel A*: Full observational and simulated data samples. For the simulated data, we show the 1-, 2-, and 3- $\sigma$  intervals. *Panel B*: Same as in the first panel but colour-coding all data point by the host galaxy’s stellar mass. If no stellar mass estimate is available for observational data points, we show them with gray symbols. *Panel C*: Same as the central panel but colour-coding the data points by the cluster formation efficiency, which is a combination of the bound fraction of star formation and the “cruel cradle effect” (Kruijssen & Cooper 2012; Kruijssen 2012) that takes the interaction of a proto-star cluster with its natal environment and nearby giant molecular clouds into account. Note that the two outliers, NGC 1705 and NGC 5238, are starburst galaxies and that their massive star clusters were previously classified as nuclear star clusters (Pechetti et al. 2020; Hoyer et al. 2021). Nuclear star clusters often exhibit complex formation histories (e.g. Spengler et al. 2017; Kacharov et al. 2018; Fahrion et al. 2021) and cannot easily be compared to our simulated star clusters.

that show a rapid half-mass radius evolution from  $\approx 0.1$  to  $\approx 1$  pc over 100 Myr. We explore different prescriptions for initial half-mass radii in Appendix A.2 but note that Reina-Campos et al. (2023a) found that none of their prescriptions, including one that depends on the local environment, can recover the  $z = 0$  distribution of the Milky Way.

The distribution of half-mass radii for old star clusters is complex and ranges from about 1 to  $\approx 25$  pc. For both galaxy morphologies the peak-structure between 5 and 10 pc is related to *in-situ* star clusters that still reside in a galaxy’s disk or were heated to the halo during galaxy mergers. The peak of the distribution has similar values for disk-dominated systems and ellipticals, which is, again, related to the properties of the galaxy’s disk. The peak is less prominent for disk-dominated systems because of a lack of major mergers.

In contrast, the broad distribution of half-mass radii is dominated by star clusters in the halo. We find that the most compact star clusters are relatively old and low-mass, approaching 13 Gyr and  $2 \times 10^3 M_\odot$ , and that the most extended clusters are younger and more massive, around 8 Gyr and  $2 \times 10^4 M_\odot$ . This difference is partly caused by different accretion histories: the more compact clusters were accreted at earlier times and experienced fewer tidal shocks, which would increase the clusters half-mass size. Observations may point towards a similar picture in that star clusters with different metallicity, and potentially of different origin, show differences in half-mass radii as well (e.g. Webb et al. 2012; Puzia et al. 2014).

Overall, we find that the properties of young star clusters are similar between galaxy morphologies. The picture becomes more complex for the old star cluster population due to their different evolutionary histories.

### 3.3. Galactocentric distances

We show the distribution of galactocentric distances of star clusters in Figure 6. We split the galaxies again into disk-dominated systems and ellipticals and into massive ( $M_* \geq 10^{10} M_\odot$ ) and dwarf ( $M_* < 10^{10} M_\odot$ ) systems. As before, star clusters are separated into young and old populations. Furthermore, we distinguish between the location of the star clusters into “halo” and “disk” components. Star clusters in disks always form *in-situ* whereas objects in the halo are either accreted from another galaxy (minor and major merger scenarios) or are heated from the disk to the halo (in case of a major merger event). All star cluster galactocentric distances are normalised by either the stellar disk scale-length for disk-dominated galaxies or the half-mass radius for ellipticals.

Our model predicts that the most distant star clusters in galaxies are all accreted and are typically old, irrespective of galaxy type and mass. On the other hand, towards galaxy centres the model predicts that the cluster population is dominated by *in-situ* and young clusters. We find that, when normalising the galactocentric distance by a mass-weighted-scale, there is no significant difference in the overall shape of the cluster distribution between different galaxy morphologies. However, when taking into account the respective scale-lengths, star clusters in more massive systems are more extended. Furthermore, in massive disk-dominated galaxies the star cluster distribution is more extended than in massive ellipticals. This trend reverses in the dwarf galaxy regime.

The old star cluster population exhibits a double-peak structure whereas the young star clusters do not. For both galaxy types this observation is explained by different star

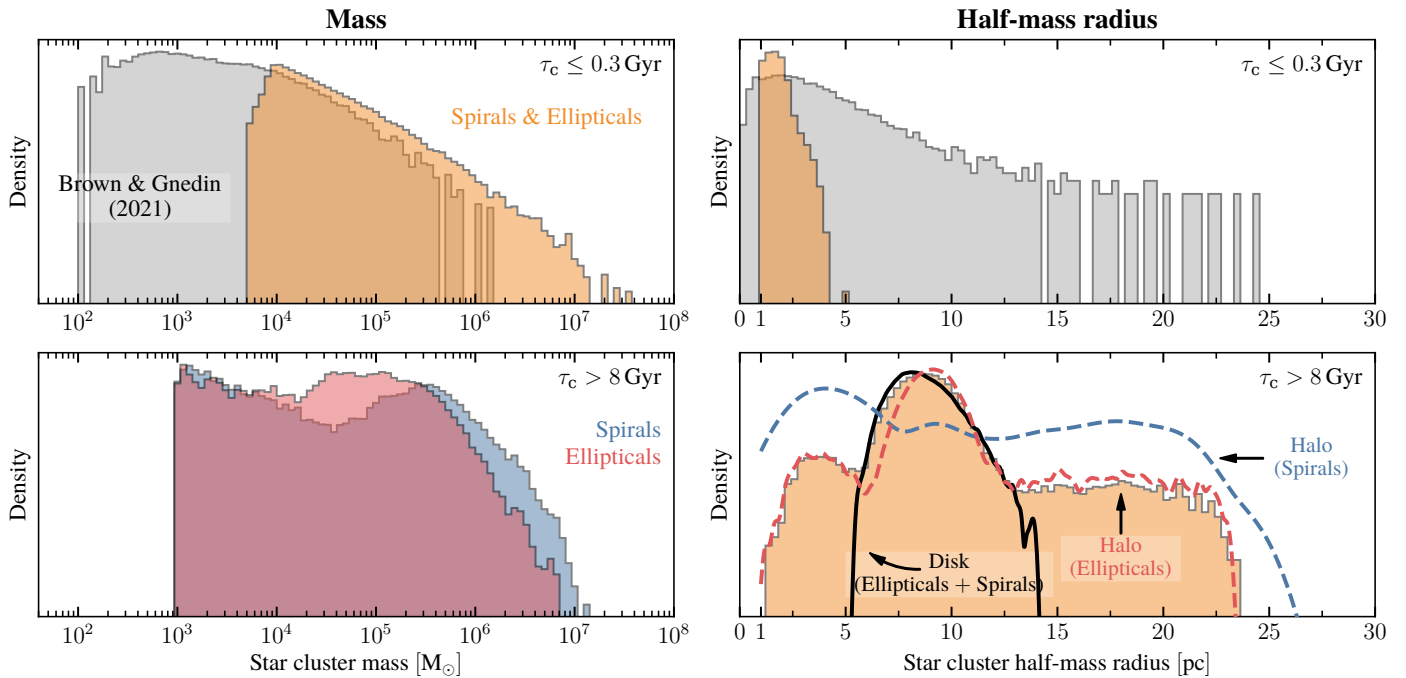


Fig. 5: *Left column*: Mass distribution of star clusters in all galaxies (orange), disk- (“spirals”; blue) and bulge-dominated (“ellipticals”; red) galaxies. The gray histogram gives the data sample of Brown & Gnedin (2021) applying an age cut of 0.3 Gyr. Star clusters are separated into young / old systems in the top / bottom row, respectively. *Right column*: Distribution of half-mass radii. The colour-coding is identical to the left panel. In the bottom panel we show the kernel density estimates for a Gaussian distribution when separating the star cluster population into the disk (solid line) and halo (dashed lines) components.

cluster origins: the inner peak is caused by old *in-situ* star clusters and the outer peak is related to accreted clusters. For disk-dominated galaxies the double-peak structure is not as prominent because they experience fewer major mergers, if any, than bulge-dominated systems.

Finally, we find that disk and halo clusters contribute equally to the total populations at relative distances of around ten. For massive disk- and bulge-dominated systems, the absolute numbers are, therefore,  $\approx 17$  and  $\approx 15$  kpc, respectively. These values are a few kpc larger than what is presented in Keller et al. (2020) for the *E-MOSAICS* simulation, however, these authors only focus on Milky Way-analogues, which may exhibit different scale-lengths than the typical disk-dominated galaxies in *L-Galaxies*. We plan to investigate the properties of the star cluster population of Milky Way-analogues in a future work.

### 3.4. Metallicity distributions

#### 3.4.1. Mean cluster metallicity

We show in Figure 7 the mean metallicity of a galaxy’s star cluster population, as traced by their iron-abundances, versus galaxy stellar mass. The iron abundance values are calculated by the galactic chemical evolution model introduced into *L-Galaxies* by Yates et al. (2013) that takes into account contributions from stellar winds and (type-Ia and -II) supernovae with different delay-time-distributions. We split the galaxies by their morphological type (disk-dominated versus elliptical; see above) and separate the star cluster population by their age (young versus old; see above).

Irrespective of the star clusters age and galaxy morphology we find that the mean metallicity increases as a function of galaxy mass, similar to the mass-metallicity relationship for galaxies (as traced via oxygen-abundances; e.g. Tremonti et al. 2004; Kewley & Ellison 2008; Torrey et al. 2019; Sanders et al. 2021). Despite some overlap younger star clusters have higher metallicity than their older counterparts at fixed stellar mass for both galaxy types. This difference appears to be more significant for disk- than for bulge-dominated galaxies, which is related to the origin of the cold gas that forms stars: in disk-dominated systems stars are predominantly formed from gas that has been continuously enriched by the above-mentioned stellar winds and supernovae channels resulting in metal-rich young star clusters. In bulge-dominated galaxies that form stars (and star clusters) a significant fraction of the cold gas comes from accreted lower-mass systems that contain relatively metal-poor gas.

We compare to the *E-MOSAICS* simulations by showing the results of the fiducial model of Pfeffer et al. (2023). Their model considers environmentally-dependent prescriptions for the cluster formation efficiency and the upper truncation mass of the cluster initial mass function, similar to what we consider for our fiducial model. The results between both simulations are in decent agreement although our data suggest higher mean metallicities at larger galaxy masses that are in better agreement with the literature. This may be a result of their poorer number statistics or different assumptions on stellar yields, resulting in other normalisation values.

We also compare our results to observational data. For disk-dominated galaxies, we consider the Milky Way and

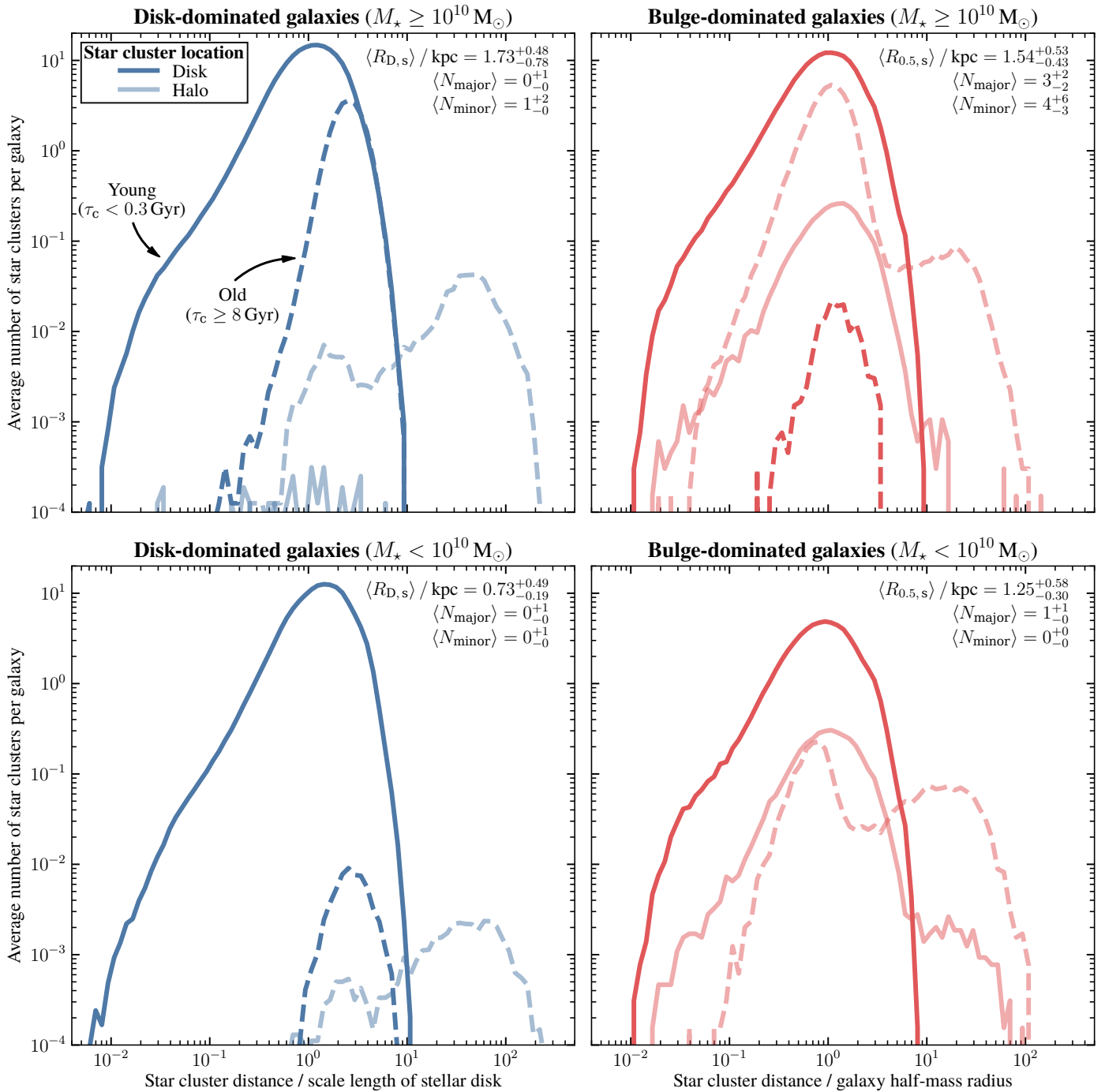


Fig. 6: Normalised galactocentric distribution of star clusters in disk-dominated (*left column*) and elliptical (*right column*) galaxies separated into massive (*top row*) and dwarf (*bottom row*) systems. Star clusters are further distinguished into young and old systems as well as their location: star clusters located in the disk are formed *in-situ* whereas objects in the halo are either accreted or re-positioned their during a major galaxy merger. The normalisation factors for disk-dominated and elliptical galaxies are the scale-length of the stellar disk and the galaxy’s half-mass radius, respectively. Each panel gives the median and 1- $\sigma$  interval for the normalisation factors and the number of major and minor mergers.

M31 as they have the most robust and quantitative measurements of globular cluster metallicities. To obtain the mean metallicity values, we collected the cluster information from a diverse set of literature that we present in a future paper (another table is presented in Pace 2024). Here we find that our simulated disk-dominated galaxies have, on average, about 0.5 dex higher median metallicity than the observed values in the Milky Way and M31, which might

be related to a lack of accreted dwarf galaxies that would contribute mainly low-metallicity star clusters.

For bulge-dominated galaxies we collect data from Usher et al. (2012); Sesto et al. (2018); Fahrian et al. (2020) and take the empirical scaling relation from Peng et al. (2006) that was fit to elliptical Virgo galaxy cluster members more massive than  $M_* = 10^9 M_\odot$ . Our simulated star cluster populations show excellent agreement with the observations

across the whole mass scale. A couple of literature data points lie outside the  $3\text{-}\sigma$  contours, which could be related to either poor number statistics of the or a bias in the ages of the star clusters in the observations with respect to our simulated galaxies.

Finally, we find that a small fraction of disk- ( $\approx 0.3\%$ ) and bulge-dominated ( $\approx 1.5\%$ ) galaxies host at least one star cluster that has  $\langle[\text{Fe}/\text{H}]\rangle < -2.5$ . This threshold is often used to indicate a “metallicity floor” due to an apparent lack of globular clusters in nearby galaxies below this value (Beasley et al. 2019). However, the detection of a low-metallicity stellar stream of a former massive star cluster in the Milky Way halo (Martin et al. 2022) and the detection of a massive star cluster with  $[\text{Fe}/\text{H}] \approx -2.9$  in M 31 (Larsen et al. 2020) challenge this notion. For M 31 specifically, our results agree with the observations, assuming that the galaxy hosts a few hundred globular clusters (Galleti et al. 2004, 2007; Huxor et al. 2008, 2014; Caldwell & Romanowsky 2016).

### 3.4.2. Bimodality

An extensive set of literature work argues that the star cluster population of many, perhaps all, galaxies shows a bi- or multi-modal colour or metallicity distribution (e.g. Cohen et al. 1998; Kundu & Whitmore 2001; Beasley et al. 2008; Brodie et al. 2012; Blom et al. 2012; Usher et al. 2012, 2013; Escudero et al. 2015; Caldwell & Romanowsky 2016; Bassino & Caso 2017; Villaume et al. 2019; Fahrion et al. 2020; Hixenbaugh et al. 2022; Lomeli-Núñez et al. 2024). An often referred to explanation is that the bi-modality is a result of different origins of clusters with the bluer (more metal-poor) population having an *ex-situ* origin (e.g. Strader et al. 2005; Brodie & Strader 2006; Katz & Ricotti 2013; Tonini 2013). Numerical work has argued that the bi- or multi-modality could be a result of either different epochs of star cluster formation, different cluster origins, as suggested by the above literature, or details related to cluster formation and destruction, or some combination thereof (see e.g. Kruijssen 2015; Choksi & Gnedin 2019). However, as pointed out by the observational work of Pastorello et al. (2015) and the numerical findings by Pfeffer et al. (2023) the bimodality may only be present in a minority ( $\lesssim 50\%$ ) of systems.

To determine the bimodality in our simulation we use an Bayesian Gaussian Mixture Model approach with Dirichlet initial conditions for all galaxies that contain more than 30 clusters. Following Muratov & Gnedin (2010) and Pfeffer et al. (2023) we first determine

$$-2 \ln \lambda = -2 \ln \left[ \frac{\max(\mathcal{L}_1)}{\max(\mathcal{L}_2)} \right], \quad (52)$$

where  $\max(\mathcal{L}_j)$  is the maximum value of the likelihood function evaluated over the metallicity distribution when considering  $j$  number of Gaussians (either one or two). Afterwards, we perform 100 bootstrap iterations to evaluate the probability that the solution is bi-modal with a probability threshold of 90%, as chosen in Pfeffer et al. (2023).<sup>8</sup> Finally, we calculate the weighted distance between the two

Gaussians,

$$D_G = \frac{|\mu_1 - \mu_2|}{\sqrt{\sigma_1^2 + \sigma_2^2}} \stackrel{!}{\geq} \sqrt{2}, \quad (53)$$

where  $\mu_j$  and  $\sigma_j$  are the mean and standard deviations of Gaussian  $j$ , respectively. If  $D_G < \sqrt{2}$ , we classify the distribution as uni-modal, as adopted in Muratov & Gnedin (2010) and Pfeffer et al. (2023).<sup>9</sup>

We show the bimodality of the star cluster distribution as a function of galaxy stellar mass in Figure 8 where we split all galaxies into disk- and bulge-dominated. Irrespective of galaxy morphology we find that the bimodal fraction (i.e. the fraction of galaxies that exhibits a bimodal metallicity distribution) is constrained to values ranging between  $\approx 30$  and  $\approx 50\%$ .

There exist some fluctuations within the data that can, in part, be attributed to galaxy merger events (e.g. the peak in ellipticals at approximately  $5 \times 10^9 M_\odot$ ) and we find some slight overall trends with metallicity: as an increasing function of galaxy stellar mass the bimodality of disk-dominated galaxies appears to slightly increase from  $\approx 35$  to  $\approx 45\%$  whereas the fraction decreases for ellipticals from  $\approx 45$  to  $\approx 40\%$ . These trends are, in part, related to the accretion history of the galaxies. The accumulated star cluster population from minor merger events typically has lower metallicity and results in a bimodal fraction. The merger history is much richer for ellipticals where we start to see that the accreted star cluster populations exhibit a wide range of metallicity values. As a result the overall metallicity distribution at  $z = 0$  extends over a large range and individual sub-structures or features become diffused. This effect can be seen in observations as well, such as massive galaxies like M 87 (see Fig. 20 in Cohen et al. 1998) or massive galaxy clusters (e.g. Harris et al. 2017).

We compare our results to the *E-MOSAICS* simulation where Pfeffer et al. (2023) performed part of the metallicity analysis. When looking at the bimodal fractions with respect to an age cut in the cluster populations, we find good agreement between the two models. The most striking difference occurs for old clusters ( $\tau_c \geq 8$  Gyr) in low-mass galaxies ( $M_\star \lesssim 5 \times 10^9 M_\odot$ ) where our data indicate a low bimodal fraction. These galaxies contain only relatively few (old) star clusters and most of them formed from gas of similar metallicity. Star cluster accretion plays a sub-dominant role because  $\approx 90\%$  of dwarf galaxies below  $M_\star \sim 5 \times 10^9 M_\odot$  are disk-dominated galaxies that have a quiet merger history.

The bimodality weakly depends on the location within a galaxy. Compared to the average bimodal fraction of all star clusters we find similarity for the inner-most galaxy regions, an increase at intermediate distances, and statistical fluctuations for the outer regions, all normalised to the disk’s scale-length and half-mass radius for disk- and bulge-dominated, respectively. This trend is a consequence of the location of accreted star clusters as the central regions are dominated by *in-situ* star clusters and the outer regions by *ex-situ* ones. The overall trend of the bimodal fraction with galaxy stellar mass remains roughly unchanged.

<sup>9</sup> Note that we do not utilise a cut on the kurtosis of the Gaussians as we find in some cases that, if there is one dominant and another sub-dominant star cluster population in a galaxy, the kurtosis is greater than zero, indicating a “peaked” distribution, thus, rejecting the hypothesis of a bimodal distribution.

<sup>8</sup> We confirmed that the random sampling of initial values during bootstrapping affects the bi-modal fractions at most by 0.05.

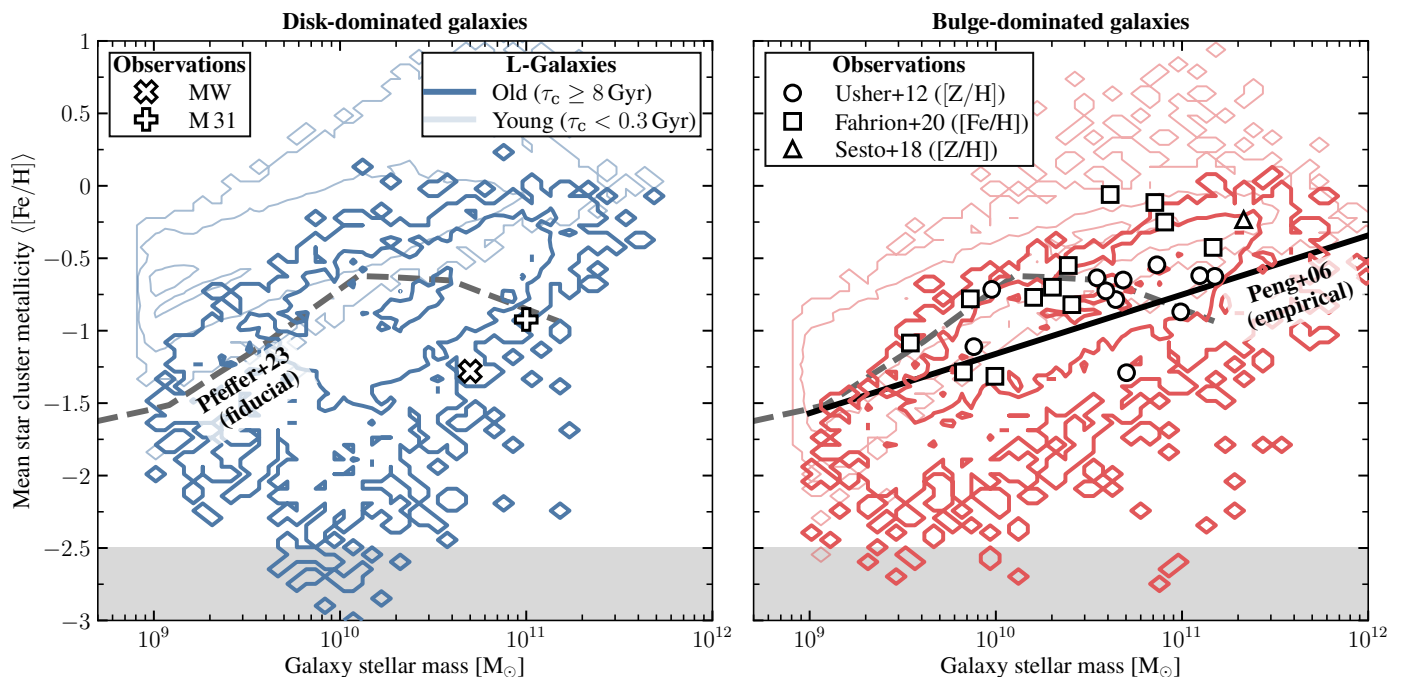


Fig. 7: Mean star cluster metallicity per galaxy versus host galaxy stellar mass, separated into disk- (*left panel*) and bulge-dominated (*right panel*) galaxies. Strong / faint contours give the 1-, 2-, and 3- $\sigma$  distribution for old / young star clusters. The gray dashed line gives the fiducial model of Pfegger et al. (2023), which assumes, similar to our model, an environmentally-dependent prescription for the upper truncation mass of the cluster initial mass function and the cluster formation efficiency. The black solid line gives the empirical relationship for ellipticals in the nearby Virgo galaxy cluster (Peng et al. 2006). Data for the Milky Way and M31 stem from a self-compiled data table that will be presented in future work. Other data points come from Usher et al. (2012), Sesto et al. (2018), and Fahrion et al. (2020). The gray-shaded area marks the “lower-limit floor” at  $\langle[\text{Fe}/\text{H}]\rangle = -2.5$  of observed star cluster metallicities in other galaxies (e.g. Beasley et al. 2019).

Our results indicate a lower bimodality when compared to observations and the general notion that a bimodal distribution appears frequently in galaxies. To test the origin of this notion and the difference we compile a list of galaxies that were classified as uni- or bimodal from the above-mentioned literature and bin the data by galaxy mass. Overall we find bimodal fractions ranging between 50 and 100%, however, galaxy number statistics are low. It appears likely that the discrepancy between these results and our simulations are due to differing methodologies and inhomogeneities when analysing data. For example, several studies consider a bimodality in the colour-distribution whereas others use iron abundances. Furthermore, taking the metallicity values of globular cluster candidates from Beasley et al. (2008) for NGC 5128 and applying our methodology results in a classification of uni-modal (because the weighted distance  $D_G$  is smaller than  $\sqrt{2}$ ) whereas the authors classify the distribution as multi-modal. Unfortunately, the metallicities of many star clusters in galaxies are not publicly available and do not allow us to test the effect of different methodologies further.

### 3.5. Caveats

Our semi-analytical approach to model star cluster populations comes with several caveats. Here we summarise a few of the most important issues.

#### 3.5.1. Axisymmetric structures of galaxies

Several effects of non-axisymmetric features can impact star clusters, some of which are discussed below. A thorough review is presented in Renaud (2018).

Some basic assumptions of *L-Galaxies* potentially break down as the gas fraction of galaxies increases, resulting in a “clumpier” structure (e.g. Conselice et al. 2004; Förster Schreiber et al. 2011; Shibuya et al. 2016). This raises some doubt about whether our model captures the properties of star clusters at redshifts of about one to two where clumpy galaxies start to make up a dominant fraction of the whole galaxy population (e.g. Sattari et al. 2023; Huertas-Company et al. 2024) and whether the  $z = 0$  star cluster population evolved in a similar fashion compared to observed star clusters. However, as argued by Ono et al. (2025) the basic principle of a disk-dominated formation scenario for galaxies may be a reasonable assumption for redshifts of  $z \gtrsim 9$ .

A related issue is that *L-Galaxies* does not consider non-axisymmetric components like bars. Molecular gas can gather at tips of the bars due to orbital crowding (Kenney & Lord 1991) leading to collisions of GMCs, triggering the formation of stars and star clusters (e.g. Davies et al. 2012; Fukui et al. 2014; Ramírez-Alegría et al. 2014). A bar can influence the dynamical evolution of star clusters as well. For instance, both Bajkova et al. (2023) and Dillamore et al. (2024) argue that the Galactic bar directly influences the orbit of a number of Milky Way globular clusters, possi-

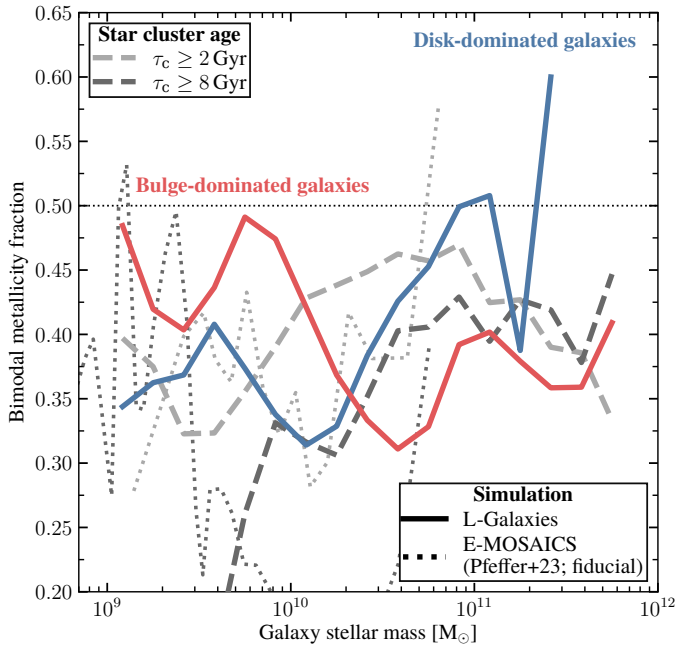


Fig. 8: Fraction of galaxies exhibiting a bimodality in the metallicity distribution of their star cluster population versus stellar mass for disk- (blue) and bulge-dominated (red) galaxies. We show the bimodality when restricting the cluster population to ages  $\tau_c \geq 2$  Gyr (light gray) and  $\tau_c \geq 8$  Gyr (dark gray) in order to compare the results to the ones for the *E-MOSAICS* simulation from Pfeffer et al. (2023, dotted lines).

bly supporting accelerating their radial migration to the Galactic Center. While halo star clusters are most likely not significantly affected by the lacking implementation of bars, objects in the galactic disk will likely be influenced, thus potentially changing the expected galactocentric distribution discussed in Section 3.3.

Finally, *L-Galaxies* does not consider the existence of spiral arms. As argued by Saha et al. (2010), (transient) spirals and bars can introduce additional energy sources for tidal heating that would increase the orthogonal velocity dispersion of star clusters compared to the orientation of the galactic disk. This effect could thus contribute star clusters to the halo of a galaxy without invoking galaxy-galaxy interactions, as indicated by the presence of metal-rich open clusters in the Milky Way’s halo (see Paunzen & Netopil 2006; Meibom et al. 2009; Brogaard et al. 2012; Heiter et al. 2014; Önehag et al. 2014; Straižys et al. 2014; Gustafsson et al. 2016; Hunt & Reffert 2023, for examples).

### 3.5.2. Impact of stellar-mass black holes

Over time, stellar mass black holes segregate towards the cluster’s centre and build up a dense core, injecting energy into the stellar system of the star cluster (e.g. Merritt et al. 2004; Mackey et al. 2008). This can result in some star clusters having relatively large half-mass radii, such as Palomar 5 (Gieles et al. 2021), rivalling the most extended objects we find in our simulation. However, note that we only consider star-star interactions in the formalism of Equation 38, thus neglecting the effect of dynamical heating due to black holes. One consequence of adding feedback from black holes is

a metallicity-dependent expansion rate that was already explored in the literature (e.g. Downing 2012; Mapelli & Bressan 2013; Banerjee 2017; Chattopadhyay et al. 2022; Rostami-Shirazi et al. 2024). This may result in a change in half-mass radii of young star clusters between different galaxy morphologies that we do not detect in Figure 5. We aim to implement this feedback channel in future versions.

### 3.5.3. Galaxy-galaxy interactions

Interactions between galaxies result in collisions between gas clouds and can cause efficient star formation outside of galaxy disks, often including the formation of star clusters (e.g. Fellhauer & Kroupa 2005; Annibali et al. 2011; Maji et al. 2017; Randriamanakoto et al. 2019; Rodruck et al. 2023). Such star clusters, especially during the first passage of the accreted galaxy, can survive for significant time and could contribute to the  $z = 0$  globular cluster population in the halo (e.g. Li et al. 2022). Keller et al. (2020) find that around 20% of globular clusters form during galaxy-galaxy merger events. If true, this would indicate that our model approach does not explain the origin of a significant fraction of globular clusters at  $z = 0$ . Nevertheless, as argued by the authors, repositioning of globular clusters from the dense inner-galactic regions into a galaxy’s halo is important for cluster survival, which matches our results.

## 4. Conclusions

We introduced a modified version of the semi-analytical galaxy formation model “*L-Galaxies*” (Henriques et al. 2020; Yates et al. 2021) that accounts for the formation of massive ( $m_c \geq 10^4 M_\odot$ ) star clusters. This implementation relies on galaxy constituents to derive the bound fraction of star formation and the total star cluster mass via *L-Galaxies*’ prescription of star formation within galaxy disks. Star cluster masses are random realisations of an environmentally-dependent cluster initial mass function, that is assumed to be a truncated power-law function, and are assigned initial half-mass radii, metallicities, and galactocentric distances. We evolve the properties of up to 2000 individual star clusters per galaxy taking into account the effects of stellar evolution, two-body relaxation, tidal shocks, dynamical friction, and a redistribution during galaxy mergers.

Running the simulation on output merger trees from the Millennium (Springel et al. 2005) and Millennium-II (Boylan-Kolchin et al. 2009) simulations yields the following results.

- The most massive and young ( $\tau_c < 0.3$  Gyr) star clusters in disk-dominated galaxies follow the observed empirical relationship between their absolute  $V$ -band magnitude of the total host galaxies star formation rate. There exist secondary dependencies on the host galaxy’s stellar mass and cluster formation efficiency; the convolved bound fraction of star formation and initial star cluster survival rate.
- The star cluster mass function for young clusters exhibits a profile similar to the observational results of nearby disk-dominated galaxies (Brown & Gnedin 2021). At the same time, the half-mass radii evolve away from the assumed constant initial value of  $r_{c,h} = 1.0$  pc up to a few parsecs but do not reproduce well the observed dis-

- tribution that exhibits a tail up to  $\approx 25$  pc. Reproducing these observations remains challenging with simulations.
- The mass, half-mass radius, and galactocentric distance functions of old ( $\tau_c \geq 8$  Gyr) star clusters display complex shapes, which results from different star cluster origins (*in-situ*, accreted, heated during galaxy mergers), and environmentally-dependent prescriptions that impact star cluster evolution. Galaxy-galaxy interactions and mergers play a vital role in shaping the properties of the  $z = 0$  star cluster population.
  - Our model is in excellent agreement with observations of the correlation between a bulge-dominated galaxy's mean star cluster metallicity, as traced by iron abundance, and its host galaxy stellar mass over four dex. This result corroborates the importance of taking into account metal enrichment of the circum-galactic medium from supernovae, as introduced in Yates et al. (2021).
  - Our results predict that the presence of a bimodality in the metallicity distribution of star clusters ranges between  $\approx 30$  and  $\approx 50\%$  of the  $z = 0$  galaxy population and does not approach 100% on any galaxy mass scale. Both different methodological approaches and the inaccessibility of a statistically significant data set of star cluster populations do not allow for a clean comparison with observations.
  - The assumption of the relationship between the sound speed of cold gas in the interstellar medium and the surface star formation rate directly influences the properties of young star clusters. For example, assuming that the turbulence in the interstellar medium is mainly related to gravity results in a slope value of the relationship between the V-band magnitude and the star formation rate being too shallow.
  - We find that the distribution of half-mass radii of old star clusters is insensitive on the prescription for the initial half-mass radii.

Our simulation offers a computationally efficient and flexible approach to probe different physical effects that influence the assembly history of star clusters across diverse galaxy populations in mass, type, and evolution over cosmic time. In future work we plan to look at additional aspects of the model, such as the star cluster properties of Milky Way analogues or their evolution with redshift, and to consider the formation of nuclear clusters as well as their interactions with (massive) black holes.

## Data availability

The code and full data output will be publicised with future papers of the series. Early access may be granted upon request.

*Acknowledgements.* NH thanks F. Belfiore, I. Cabrera-Ziri, M. Gieles, J. Greene, J. Lee, M. Mapelli, D. Maschmann, T. Naab, M. Reina-Campos, A. Seth, V. Springel, and S. Tornamenti for useful discussions. NH is a Fellow of the International Max Planck Research School for Astronomy and Cosmic Physics at the University of Heidelberg (IMPRS-HD) and acknowledges their support. NH acknowledges funding through LACEGAL, a Latinamerican Chinese European Galaxy Formation Network. This project has received funding from the European Union's HORIZON-MSCA-2021-SE-01 Research and Innovation programme under the Marie Skłodowska-Curie grant agreement number 101086388. S.B. acknowledges support from the Spanish Ministerio de Ciencia e Innovación through project PID2021-124243NB-C21 DS acknowledges the support by the Tsinghua Shui Mu Scholarship, the funding of the National Key R&D Program of China (grant No.

2023YFA1605600), the science research grants from the China Manned Space Project with No. CMS-CSST2021-A05, and the Tsinghua University Initiative Scientific Research Program (No. 0223080023). MCA acknowledges support from Fondecyt Iniciación #11240540.

## References

- Adamo, A., Bradley, L. D., Vanzella, E., et al. 2024, *Nature*, 632, 513
- Adamo, A., Kruijssen, J. M. D., Bastian, N., Silva-Villa, E., & Ryon, J. 2015, *MNRAS*, 452, 246
- Adamo, A., Östlin, G., & Zackrisson, E. 2011, *MNRAS*, 417, 1904
- Adamo, A., Ryon, J. E., Messa, M., et al. 2017, *The Astrophysical Journal*, 841, 131
- Alexander, P. E. R. & Gieles, M. 2012, *MNRAS*, 422, 3415
- Alexander, P. E. R., Gieles, M., Lamers, H. J. G. L. M., & Baumgardt, H. 2014, *MNRAS*, 442, 1265
- Andersson, E. P., Mac Low, M.-M., Agertz, O., Renaud, F., & Li, H. 2024, *Astronomy & Astrophysics*, 681, A28
- Angulo, R. E. & Hilbert, S. 2015, *MNRAS*, 448, 364
- Angulo, R. E. & White, S. D. M. 2010, *MNRAS*, 405, 143
- Annibali, F., Tosi, M., Aloisi, A., & van der Marel, R. P. 2011, *The Astronomical Journal*, 142, 129
- Annibali, F., Tosi, M., Monelli, M., et al. 2009, *The Astronomical Journal*, 138, 169
- Ayromlou, M., Kauffmann, G., Yates, R. M., Nelson, D., & White, S. D. M. 2021, *MNRAS*, 505, 492
- Bajkova, A. T., Smirnov, A. A., & Bobylev, V. V. 2023, *Astrophysical Bulletin*, 78, 499
- Banerjee, S. 2017, *MNRAS*, 467, 524
- Banerjee, S. & Kroupa, P. 2017, *Astronomy & Astrophysics*, 597, A28
- Barmby, P. & Huchra, J. P. 2001, *The Astronomical Journal*, 122, 2458
- Barmby, P., Huchra, J. P., Brodie, J. P., et al. 2000, *The Astronomical Journal*, 119, 727
- Barrera, M., Springel, V., White, S. D. M., et al. 2023, *MNRAS*, 525, 6312
- Bassino, L. P. & Caso, J. P. 2017, *MNRAS*, 466, 4259
- Bastian, N. 2008, *MNRAS*, 390, 759
- Bastian, N., Adamo, A., Gieles, M., et al. 2012, *MNRAS*, 419, 2606
- Bastian, N., Pfeffer, J., Kruijssen, J. M. D., et al. 2020, *MNRAS*, 498, 1050
- Baugh, C. M. 2006, *Reports on Progress in Physics*, 69, 3101
- Baumgardt, H. & Hilker, M. 2018, *MNRAS*, 478, 1520
- Beasley, M. A., Bridges, T., Peng, E., et al. 2008, *MNRAS*, 386, 1443
- Beasley, M. A., Leaman, R., Gallart, C., et al. 2019, *MNRAS*, 487, 1986
- Bertin, G. & Romeo, A. B. 1988, *Astronomy & Astrophysics*, 195, 105
- Bertoldi, F. & McKee, C. F. 1992, *The Astrophysical Journal*, 395, 140
- Bik, A., Lamers, H. J. G. L. M., Bastian, N., Panagia, N., & Romaniello, M. 2003, *Astronomy & Astrophysics*, 397, 473
- Binney, J. & Tremaine, S. 2008, *Galactic Dynamics: Second Edition* (Princeton University Press)
- Blakeslee, J. P. 1999, *The Astronomical Journal*, 118, 1506
- Blom, C., Spitler, L. R., & Forbes, D. A. 2012, *MNRAS*, 420, 37
- Bluck, A. F. L., Mendel, T. J., Ellison, S. L., et al. 2016, *MNRAS*, 462, 2559
- Bonoli, S., Marulli, F., Springel, V., et al. 2009, *MNRAS*, 396, 423
- Bonoli, S., Mayer, L., & Callegari, S. 2014, *MNRAS*, 437, 1576
- Bottema, R. 1993, *Astronomy & Astrophysics*, 275, 16
- Boylan-Kolchin, M., Springel, V., White, S. D. M., Jenkins, A., & Lemson, G. 2009, *MNRAS*, 398, 1150
- Bradley, L. D., Adamo, A., Vanzella, E., et al. 2024, *The Astrophysical Journal*, 22
- Brodie, J. P. & Strader, J. 2006, *Annual Review of Astronomy & Astrophysics*, 44, 193
- Brodie, J. P., Usher, C., Conroy, C., et al. 2012, *The Astrophysical Journal Letters*, 759, L33
- Brogaard, K., VandenBerg, D. A., Bruntt, H., et al. 2012, *Astronomy & Astrophysics*, 543, A106
- Brown, G. & Gnedin, O. Y. 2021, *MNRAS*, 508, 5935
- Brown, G. & Gnedin, O. Y. 2022, *MNRAS*, 514, 280
- Burkert, A. & Forbes, D. A. 2020, *The Astronomical Journal*, 159, 56
- Burkhart, B. 2018, *The Astrophysical Journal*, 863, 118
- Caldwell, N. & Romanowsky, A. J. 2016, *The Astrophysical Journal*, 824, 42
- Callingham, T. M., Cautun, M., Deason, A. J., et al. 2022, *MNRAS*, 513, 4107

- Calura, F., Pascale, R., Agertz, O., et al. 2024, arXiv e-prints, arXiv:2411.02502
- Calzetti, D., Lee, J. C., Sabbi, E., et al. 2015, *The Astronomical Journal*, 149, 51
- Cantiello, M., Capaccioli, M., Napolitano, N., et al. 2015, *Astronomy & Astrophysics*, 576, A14
- Carretta, E., Gratton, R. G., Clementini, G., & Fusi Pecci, F. 2000, *The Astrophysical Journal*, 533, 215
- Chabrier, G. 2003, *The Publications of the Astronomical Society of the Pacific*, 115, 763
- Chandrasekhar, S. 1943, *The Astrophysical Journal*, 97, 255
- Chattopadhyay, D., Hurley, J., Stevenson, S., & Raidani, A. 2022, *MNRAS*, 513, 4527
- Chevané, M., Kruijssen, J. M. D., Hygate, A. P. S., et al. 2020, *MNRAS*, 493, 2872
- Choksi, N., Behroozi, P., Volonteri, M., et al. 2017, *MNRAS*, 472, 1526
- Choksi, N. & Gnedin, O. Y. 2019, *MNRAS*, 486, 331
- Choksi, N. & Kruijssen, J. M. D. 2021, *MNRAS*, 507, 5492
- Claeysens, A., Adamo, A., Richard, J., et al. 2023, *MNRAS*, 520, 2180
- Cohen, J. G., Blakeslee, J. P., & Ryzhov, A. 1998, *The Astrophysical Journal*, 496, 808
- Colombo, D., Hughes, A., Schinnerer, E., et al. 2014, *The Astrophysical Journal*, 784, 3
- Conroy, C. & Gunn, J. E. 2010a, FSPS: Flexible Stellar Population Synthesis, *Astrophysics Source Code Library*, record ascl:1010.043
- Conroy, C. & Gunn, J. E. 2010b, *The Astrophysical Journal*, 712, 833
- Conroy, C., Gunn, J. E., & White, M. 2009, *The Astrophysical Journal*, 699, 486
- Conroy, C., White, M., & Gunn, J. E. 2010, *The Astrophysical Journal*, 708, 58
- Conselice, C. J., Grogin, N. A., Joglekar, S., et al. 2004, *The Astrophysical Journal Letters*, 600, L139
- Cook, D. O., Lee, J. C., Adamo, A., et al. 2023, *MNRAS*, 519, 3749
- Cook, D. O., Seth, A. C., Dale, D. A., et al. 2012, *The Astrophysical Journal*, 751, 100
- Correnti, M., Gennaro, M., Kalirai, J. S., Brown, T. M., & Calamida, A. 2016, *The Astrophysical Journal*, 823, 18
- Crain, R. A., Schaye, J., Bower, R. G., et al. 2015, *MNRAS*, 450, 1937
- Croton, D. J. 2006, *MNRAS*, 369, 1808
- Croton, D. J., Springel, V., White, S. D. M., et al. 2006, *MNRAS*, 365, 11
- da Silva, R. L., Fumagalli, M., & Krumholz, M. 2012, *The Astrophysical Journal*, 745, 145
- da Silva, R. L., Fumagalli, M., & Krumholz, M. 2014, *MNRAS*, 444, 3275
- Davies, B., de La Fuente, D., Najarro, F., et al. 2012, *MNRAS*, 419, 1860
- Davis, M., Efstathiou, G., Frenk, C. S., & White, S. D. M. 1985, *The Astrophysical Journal*, 292, 371
- De Lucia, G. & Blaizot, J. 2007, *MNRAS*, 375, 2
- De Lucia, G., Kruijssen, J. M. D., Trujillo-Gomez, S., Hirschmann, M., & Xie, L. 2024, *MNRAS*, 530, 2760
- De Lucia, G., Tornatore, L., Frenk, C. S., et al. 2014, *MNRAS*, 445, 970
- del P. Lagos, C., Bravo, M., Tobar, R., et al. 2024, *MNRAS*, 531, 3551
- Dillamore, A. M., Monty, S., Belokurov, V., & Evans, N. W. 2024, *The Astrophysical Journal Letters*, 971, L4
- Dobbs, C. L., Burkert, A., & Pringle, J. E. 2011, *MNRAS*, 417, 1318
- Dolag, K., Borgani, S., Murante, G., & Springel, V. 2009, *MNRAS*, 399, 497
- Dolfi, A., Pfeffer, J., Forbes, D. A., et al. 2022, *MNRAS*, 511, 3179
- Downing, J. M. B. 2012, *MNRAS*, 425, 2234
- Dutton, A. A. & Macció, A. V. 2014, *MNRAS*, 441, 3359
- Ekström, S., Georgy, C., Eggenberger, P., et al. 2012, *Astronomy & Astrophysics*, 537, A146
- El-Badry, K., Quataert, E., Weisz, D. R., Choksi, N., & Boylan-Kolchin, M. 2019, *MNRAS*, 482, 4528
- Elmegreen, B. & Lahén, N. 2024, *The Open Journal of Astrophysics*, 7, 68
- Elmegreen, D. M., Elmegreen, B. G., Ravindranath, S., & Coe, D. A. 2007, *The Astrophysical Journal*, 658, 763
- Emig, K. L., Bolatto, A. D., Leroy, A. K., et al. 2020, *The Astrophysical Journal*, 903, 50
- Emsellem, E., Schinnerer, E., Santoro, F., et al. 2022, *Astronomy & Astrophysics*, 659, A191
- Escala, A., Larson, R. B., Coppi, P. S., & Mardones, D. 2004, *The Astrophysical Journal*, 607, 765
- Escudero, C. G., Faifer, F. R., Bassino, L. P., Calderón, J. P., & Caso, J. P. 2015, *MNRAS*, 449, 612
- Fahrion, K., Lyubenova, M., Hilker, M., et al. 2020, *Astronomy & Astrophysics*, 637, A26
- Fahrion, K., Lyubenova, M., van de Ven, G., et al. 2021, *Astronomy & Astrophysics*, 650, A137
- Fellhauer, M. & Kroupa, P. 2005, *Monthly Notices of the Royal Astronomical Society*, 359, 223
- Feng, C.-C., Lin, L.-H., Wang, H.-H., & Taam, R. E. 2014, *The Astrophysical Journal*, 785, 103
- Filion, C., McClure, R. L., Weinberg, M. D., D'Onghia, E., & Daniel, K. J. 2023, *MNRAS*, 524, 276
- Flynn, C., Holmberg, J., Portinari, L., Fuchs, B., & Jahreiß, H. 2006, *MNRAS*, 372, 1149
- Forbes, D. A., Bastian, N., Gieles, M., et al. 2018, *Proceedings of the Royal Society of London Series A*, 474, 20170616
- Forbes, D. A. & Bridges, T. 2010, *MNRAS*, 404, 1203
- Forbes, D. A. & Romanowsky, A. J. 2023, *MNRAS*, 520, L58
- Förster Schreiber, N. M., Shapley, A. E., Erb, D. K., et al. 2011, *The Astrophysical Journal*, 731, 65
- Freeman, K. C. 1970, *The Astrophysical Journal*, 160, 811
- Fu, J., Guo, Q., Kauffmann, G., & Krumholz, M. R. 2010, *MNRAS*, 409, 515
- Fu, J., Kauffmann, G., Huang, M.-L., et al. 2013, *MNRAS*, 434, 1531
- Fu, J., Kauffmann, G., Li, C., & Qi, G. 2012, *MNRAS*, 424, 2701
- Fukui, Y., Ohama, A., Hanaoka, N., et al. 2014, *The Astrophysical Journal*, 780, 36
- Gabrielpillai, A., Somerville, R. S., Genel, S., et al. 2022, *MNRAS*, 517, 6091
- Galleti, S., Bellazzini, M., Federici, L., Buzzoni, A., & Fusi Pecci, F. 2007, *Astronomy & Astrophysics*, 471, 127
- Galleti, S., Federici, L., Bellazzini, M., Fusi Pecci, F., & Macrina, S. 2004, *Astronomy & Astrophysics*, 416, 917
- García, F. A. B., Ricotti, M., Sugimura, K., & Park, J. 2023, *Monthly Notices of the Royal Astronomical Society*, 522, 2495
- Garro, E. R., Minniti, D., & Fernández-Trincado, J. G. 2024, *Astronomy & Astrophysics*, 687, A214
- Genzel, R., Newman, S., Jones, T., et al. 2011, *The Astrophysical Journal*, 733, 101
- Georgy, C., Ekström, S., Eggenberger, P., et al. 2013, *Astronomy & Astrophysics*, 558, A103
- Gieles, M., Erkal, D., Antonini, F., Balbinot, E., & Peñarrubia, J. 2021, *Nature Astronomy*, 5, 957
- Gieles, M., Hogg, D. C., & Zhao, H. 2011, *MNRAS*, 413, 2509
- Gieles, M. & Renaud, F. 2016, *MNRAS*, 463, L103
- Giersz, M., Askar, A., Wang, L., et al. 2019, *MNRAS*, 487, 2412
- Giersz, M. & Hogg, D. C. 1994, *MNRAS*, 268, 257
- Goddard, Q. E., Bastian, N., & Kennicutt, R. C. 2010, *MNRAS*, 405, 857
- Green, A. W., Glazebrook, K., McGregor, P. J., et al. 2014, *MNRAS*, 437, 1070
- Guo, Q., White, S., Boylan-Kolchin, M., et al. 2011, *MNRAS*, 413, 101
- Guo, S. & Qi, Z. 2023, *Universe*, 9, 252
- Gustafsson, B., Church, R. P., Davies, M. B., & Rickman, H. 2016, *Astronomy & Astrophysics*, 593, A85
- Hackshaw, Z., Hawkins, K., Filion, C., et al. 2024, *The Astrophysical Journal*, 19
- Hammer, F., Li, H., Mamon, G. A., et al. 2023, *MNRAS*, 519, 5059
- Hammer, F., Wang, J., Mamon, G. A., et al. 2024, *MNRAS*, 527, 2718
- Harris, W. E., Ciccone, S. M., Eadie, G. M., et al. 2017, *The Astrophysical Journal*, 835, 101
- Hawkins, K. 2023, *MNRAS*, 525, 3318
- Heiter, U., Soubiran, C., Netopil, M., & Paunzen, E. 2014, *Astronomy & Astrophysics*, 561, A93
- Hénon, M. 1961, *Annales d'Astrophysique*, 24, 369
- Henriques, B. M. B., White, S. D. M., Thomas, P. A., et al. 2015, *MNRAS*, 451, 2663
- Henriques, B. M. B., Yates, R. M., Fu, J., et al. 2020, *MNRAS*, 491, 5795
- Heyer, M., Krawczyk, C., Duval, J., & Jackson, J. M. 2009, *The Astrophysical Journal*, 699, 1092
- Heyer, M. H., Corbelli, E., Schneider, S. E., & Young, J. S. 2004, *The Astrophysical Journal*, 602, 723
- Hirschmann, M., De Lucia, G., & Fontanot, F. 2016, *MNRAS*, 461, 1760
- Hislop, J. M., Naab, T., Steinwandel, U. P., et al. 2022, *MNRAS*, 509, 5938
- Hixenbaugh, K., Chandar, P., & Mok, A. 2022, *The Astronomical Journal*, 163, 271

- Ho, I.-T., Kreckel, K., Meidt, S. E., et al. 2019, *The Astrophysical Journal Letters*, 885, L31
- Ho, I.-T., Seibert, M., Meidt, S. E., et al. 2017, *The Astrophysical Journal*, 846, 39
- Hopkins, P. F., Quataert, E., & Murray, N. 2012, *MNRAS*, 421, 3488
- Horta, D., Hughes, M. E., Pfeffer, J. L., et al. 2011, *MNRAS*, 500, 4768
- Hoyer, N., Neumayer, N., Georgiev, I. Y., Seth, A. C., & Greene, J. E. 2021, *MNRAS*, 507, 3246
- Huchra, J. P., Brodie, J. P., & Kent, S. M. 1991, *The Astrophysical Journal*, 370, 495
- Hudson, M. J., Harris, G. L., & Harris, W. E. 2014, *The Astrophysical Journal Letters*, 787, L5
- Huertas-Company, M., Iyer, K. G., Angeloudi, E., et al. 2024, *Astronomy & Astrophysics*, 685, A48
- Hughes, M. E., Pfeffer, J., Martig, M., et al. 2019, *MNRAS*, 482, 2795
- Hughes, M. E., Pfeffer, J. L., Bastian, N., et al. 2022, *MNRAS*, 510, 6190
- Hughes, M. E., Pfeffer, J. L., Martig, M., et al. 2020, *MNRAS*, 491, 4012
- Hunt, E. L. & Reffert, S. 2023, *Astronomy & Astrophysics*, 673, A114
- Hunter, D. A., Elmegreen, B. G., Dupuy, T. J., & Mortonson, M. 2003, *The Astronomical Journal*, 126, 1836
- Huxor, A. P., Mackey, A. D., Ferguson, A. M. N., et al. 2014, *MNRAS*, 442, 2165
- Huxor, A. P., Tanvir, N. R., Ferguson, A. M. N., et al. 2008, *MNRAS*, 385, 1989
- Hwang, H.-C., Barrera-Ballesteros, J. K., Heckman, T. M., et al. 2019, *The Astrophysical Journal*, 872, 144
- Ines Ennis, A., Caso, J. P., & Bassino, L. P. 2024, *The Open Journal of Astrophysics*, 12
- Irodoutou, D., Thomas, P. A., Henriques, B. M. B., Sargent, M. T., & Hislop, J. M. 2019, *MNRAS*, 489, 3609
- Izquierdo-Villalba, D., Bonoli, S., Dotti, M., et al. 2020, *MNRAS*, 495, 4681
- Izquierdo-Villalba, D., Bonoli, S., Spinoso, D., et al. 2019, *MNRAS*, 488, 609
- Izquierdo-Villalba, D., Sesana, A., Bonoli, S., & Colpi, M. 2022, *MNRAS*, 509, 3488
- Jaffe, W. 1983, *MNRAS*, 202, 995
- Johnson, B., Foreman-Mackey, D., Sick, J., et al. 2023, *python-fsps*
- Johnson, K. E., Leitherer, C., Vacca, W. D., & Conti, P. S. 2000, *The Astronomical Journal*, 120, 1273
- Kacharov, N., Neumayer, N., Seth, A. C., et al. 2018, *MNRAS*, 480, 1973
- Karam, J. & Sills, A. 2022, *MNRAS*, 513, 6095
- Karam, J. & Sills, A. 2023, *MNRAS*, 521, 5557
- Katz, H. & Ricotti, M. 2013, *MNRAS*, 432, 3250
- Kauffmann, G. & Haehnelt, M. 2000, *MNRAS*, 311, 576
- Kaviraj, S., Ferreras, I., Yoon, S.-J., & Yi, S. K. 2005, *Astronomy & Astrophysics*, 439, 913
- Keller, B. W., Kruijssen, J. M. D., Pfeffer, J., et al. 2020, *MNRAS*, 495, 4248
- Kenney, J. D. P. & Lord, S. D. 1991, *The Astrophysical Journal*, 381, 118
- Kennicutt, R. C. 1998, *Annual Review of Astronomy and Astrophysics*, 36, 189
- Kewley, L. J. & Ellison, S. L. 2008, *The Astrophysical Journal*, 681, 1183
- Kikuchi, S., Ouchi, M., Ono, Y., et al. 2020, *The Astrophysical Journal*, 893, 60
- King, I. 1962, *The Astronomical Journal*, 67, 471
- Krauss, L. M. & Chaboyer, B. 2003, *Science*, 229, 65
- Kravtsov, A. V. & Gnedin, O. Y. 2005, *The Astrophysical Journal*, 623, 650
- Kreckel, K., Ho, I.-T., Blanc, G. A., et al. 2019, *The Astrophysical Journal*, 887, 80
- Kritsuk, A. G., Norman, M. L., Padoan, P., & Wagner, R. 2007, *The Astrophysical Journal*, 665, 416
- Kritsuk, A. G., Ustyugov, S. D., & Norman, M. L. 2017, *New Journal of Physics*, 19, 065003
- Kruijssen, J. M. D. 2012, *MNRAS*, 426, 3008
- Kruijssen, J. M. D. 2014, *Classical and Quantum Gravity*, 31, 244006
- Kruijssen, J. M. D. 2015, *MNRAS*, 454, 1658
- Kruijssen, J. M. D. & Cooper, A. P. 2012, *MNRAS*, 420, 340
- Kruijssen, J. M. D., Pfeffer, J. L., Chevance, M., et al. 2020, *MNRAS*, 498, 2472
- Kruijssen, J. M. D., Pfeffer, J. L., Crain, R. A., & Bastian, N. 2019a, *MNRAS*, 486, 3134
- Kruijssen, J. M. D., Pfeffer, J. L., Reina-Campos, M., Crain, R. A., & Bastian, N. 2019b, *MNRAS*, 486, 3180
- Krumholz, M. R. & Burkhardt, B. 2016, *MNRAS*, 458, 1671
- Krumholz, M. R., Burkhardt, B., Forbes, J. C., & Crocker, R. M. 2018, *MNRAS*, 477, 2716
- Krumholz, M. R., Fumagalli, M., da Silva, R. L., Rendahl, T., & Parra, J. 2015, *MNRAS*, 452, 1447
- Krumholz, M. R. & McKee, C. F. 2005, *The Astrophysical Journal*, 630, 260
- Krumholz, M. R., McKee, C. F., & Tumlinson, J. 2009, *The Astrophysical Journal*, 693, 216
- Kuijken, K. & Gilmore, G. 1989, *MNRAS*, 239, 571
- Kundu, A. & Whitmore, B. C. 2001, *The Astronomical Journal*, 121, 2950
- Lahén, N., Naab, T., Johansson, P. H., et al. 2020, *The Astrophysical Journal*, 891, 2
- Lahén, N., Naab, T., Kauffmann, G., et al. 2023, *MNRAS*, 522, 3092
- Lahén, N., Naab, T., & Szécsi, D. 2024a, *MNRAS*, 530, 645
- Lahén, N., Rantala, A., Naab, T., et al. 2024b, *arXiv e-prints*, arXiv:2410.01891
- Lake, W., Naoz, S., Marinacci, F., et al. 2023, *The Astrophysical Journal Letters*, 956, L7
- Lake, W., Naoz, S., Chiou, Y. S., et al. 2021, *The Astrophysical Journal*, 922, 86
- Lamers, H. J. G. L. M., Gieles, M., & Portegies Zwart, S. F. 2005, *Astronomy & Astrophysics*, 429, 173
- Larsen, S. S. 2002, *The Astronomical Journal*, 124, 1393
- Larsen, S. S. 2010, *Philosophical Transactions of the Royal Society of London Series A*, 368, 867
- Larsen, S. S., Romanowsky, A. J., Brodie, J. P., & Wasserman, A. 2020, *Science*, 370, 970
- Larson, R. B. 1981, *MNRAS*, 194, 809
- Le, M. N. & Cooper, A. P. 2024, *The Astrophysical Journal*, 26
- Leaman, R., VandenBerg, D. A., & Mendel, J. T. 2013, *MNRAS*, 436, 122
- Lee, J. C., Sandstrom, K. M., Leroy, A. K., et al. 2023, *The Astrophysical Journal Letters*, 944, L17
- Lee, J. C., Whitmore, B. C., Thilker, D. A., et al. 2022, *The Astrophysical Journal Series*, 258, 10
- Lee, M. G. 2003, *Journal of Korean Astronomical Society*, 36, 189
- Lehnert, M. D., Nesvadba, N. P. H., Le Tiran, L., et al. 2009, *The Astrophysical Journal*, 699, 1660
- Leroy, A. K., Walter, F., Brinks, E., et al. 2008, *The Astronomical Journal*, 136, 2782
- Levy, R. C., Bolatto, A. D., Mayya, D., et al. 2024, *The Astrophysical Journal Letters*, 16
- Li, H. & Gnedin, O. Y. 2019, *MNRAS*, 486, 4030
- Li, H., Gnedin, O. Y., & Gnedin, N. Y. 2018, *The Astrophysical Journal*, 861, 107
- Li, H., Gnedin, O. Y., Gnedin, N. Y., et al. 2017, *The Astrophysical Journal*, 834, 69
- Li, H., Vogelberger, M., Bryan, G. L., et al. 2022, *MNRAS*, 514, 265
- Lim, S. & Lee, M. G. 2015, *The Astrophysical Journal*, 804, 123
- Lin, C. C. & Shu, F. H. 1966, *Proceedings of the National Academy of Science*, 55, 229
- Lomeli-Núñez, L., Mayya, Y. D., Rodríguez-Merino, L. H., et al. 2024, *MNRAS*, 528, 1445
- Mackey, A. D., Wilkinson, M. I., Davies, M. B., & Gilmore, G. F. 2008, *MNRAS*, 386, 65
- Mai, Y., Croom, S. M., Wisnioski, E., et al. 2024, *MNRAS*, 15
- Maji, M., Zhu, Q., Li, Y., et al. 2017, *The Astrophysical Journal*, 844, 108
- Mapelli, M. & Bressan, A. 2013, *MNRAS*, 430, 3120
- Maraston, C., Bastian, N., Saglia, R. P., et al. 2004, *Astronomy & Astrophysics*, 416, 467
- Martin, N. F., Venn, K. A., Aguado, D. S., et al. 2022, *Nature*, 601, 45
- Maschmann, D., Lee, J. C., Thilker, D. A., et al. 2024, *The Astrophysical Journal Supplement Series*, 273, 14
- Matzner, C. D. & McKee, C. F. 2000, *The Astrophysical Journal*, 545, 364
- McCradly, N. & Graham, J. R. 2007, *The Astrophysical Journal*, 663, 844
- McKee, C. F. & Krumholz, M. R. 2010, *The Astrophysical Journal*, 709, 308
- McKee, C. F. & Tan, J. C. 2003, *The Astrophysical Journal*, 585, 850
- Meibom, S., Grundahl, F., Clausen, J. V., et al. 2009, *The Astronomical Journal*, 137, 5086
- Merritt, D., Piatek, S., Portegies Zwart, S., & Hemsendorf, M. 2004, *The Astrophysical Journal Letters*, 608, L25
- Metha, B., Trenti, M., Battisti, A., & Chu, T. 2024, *MNRAS*, 529, 104

- Metha, B., Trenti, M., & Chu, T. 2021, *MNRAS*, 508, 489
- Meynet, G., Maeder, A., Schaller, G., Schaerer, D., & Charbonnel, C. 1994, *Astronomy & Astrophysics Supplement Series*, 103, 97
- Minniti, D., Geisler, D., Alonso-García, J., et al. 2017, *The Astrophysical Journal Letters*, 849, L24
- Monaco, P., Fontanot, F., & Taffoni, G. 2007, *MNRAS*, 375, 1189
- Mowla, L., Iyer, K., Asada, Y., et al. 2024, arXiv e-prints, arXiv:2402.08696
- Mowla, L., Iyer, K. G., Desprez, G., et al. 2022, *The Astrophysical Journal Letters*, 937, L35
- Muratov, A. L. & Gnedin, O. Y. 2010, *The Astrophysical Journal*, 718, 1266
- Murphy, G. G., Yates, R. M., & Mohamed, S. S. 2022, *MNRAS*, 510, 1945
- Myeong, G. C., Evans, N. W., Belokurov, V., Sanders, L. J., & Koposov, S. E. 2018, *The Astrophysical Journal Letters*, 863, L28
- Myers, P. C. & Goodman, A. A. 1988, *The Astrophysical Journal*, 329, 392
- Navarro, J. F., Frenk, C. S., & White, S. D. M. 1996, *The Astrophysical Journal*, 462, 563
- Newton, O., Davies, J. J., Pfeffer, J., et al. 2024, arXiv, 17
- Nordlund, Å. & Padoan, P. 1999, in *Interstellar Turbulence*, ed. J. Franco & A. Carraminana, 218
- Ohlson, D., Seth, A. C., Gallo, E., Baldassare, V. F., & Greene, J. E. 2023, *The Astronomical Journal*, 23
- Oklopčić, A., Hopkins, P. F., Feldmann, R., et al. 2017, *MNRAS*, 465, 952
- Önehag, A., Gustafsson, B., & Korn, A. 2014, *Astronomy & Astrophysics*, 562, A102
- Ono, Y., Ouchi, M., Harikane, Y., et al. 2025, arXiv e-prints, 24
- Ostriker, E. C. 1999, *The Astrophysical Journal*, 513, 252
- Ostriker, E. C., Stone, J. M., & Gammie, C. F. 2001, *The Astrophysical Journal*, 546, 980
- Pace, A. B. 2024, arXiv e-prints, arXiv:2411.07424
- Padoan, P., Jimenez, R., & Jones, B. 1997, *MNRAS*, 185, 711
- Padoan, P. & Nordlund, Å. 2002, *The Astrophysical Journal*, 576, 870
- Padoan, P. & Nordlund, Å. 2011, *The Astrophysical Journal*, 730, 40
- Parente, M., Ragone-Figueroa, C., Granato, G. L., & Lapi, A. 2023, *MNRAS*, 521, 6105
- Parente, M., Ragone-Figueroa, C., López, P., et al. 2024, *The Astrophysical Journal*, 966, 154
- Pasquali, A., Bik, A., Zibetti, S., et al. 2011, *The Astronomical Journal*, 141, 132
- Pastorello, N., Forbes, D. A., Usher, C., et al. 2015, *MNRAS*, 451, 2625
- Paunzen, E. & Netopil, M. 2006, *MNRAS*, 371, 1641
- Pechetti, R., Seth, A. C., Neumayer, N., et al. 2020, *The Astrophysical Journal*, 900, 32
- Peng, E. W., Jordán, A., Côté, P., et al. 2006, *The Astrophysical Journal*, 639, 95
- Peng, E. W., Jordán, A., Côté, P., et al. 2008, *The Astrophysical Journal*, 681, 197
- Perrett, K. M., Bridges, T. J., Hanes, D. A., et al. 2002, *The Astronomical Journal*, 123, 2490
- Pfeffer, J., Bastian, N., Crain, R. A., et al. 2019a, *MNRAS*, 487, 4550
- Pfeffer, J., Bastian, N., Kruijssen, J. M. D., et al. 2019b, *MNRAS*, 490, 1714
- Pfeffer, J., Forbes, D. A., Romanowsky, A. J., et al. 2024a, arXiv e-prints, arXiv:2410.07498
- Pfeffer, J., Janssens, S. R., Buzzo, M. L., et al. 2024b, *MNRAS*, 429, 4914
- Pfeffer, J., Kruijssen, J. M. D., Bastian, N., Crain, R. A., & Trujillo-Gomez, S. 2023, *MNRAS*, 519, 5384
- Pfeffer, J., Kruijssen, J. M. D., Crain, R. A., & Bastian, N. 2018, *MNRAS*, 475, 4309
- Planck Collaboration. 2014, *Astronomy & Astrophysics*, 571, A16
- Plummer, H. C. 1911, *MNRAS*, 71, 460
- Poggio, E., Recio-Blanco, A., Palicio, P. A., et al. 2022, *Astronomy & Astrophysics*, 666, L4
- Polkas, M., Bonoli, S., Bortolas, E., et al. 2024, *Astronomy & Astrophysics*, 689, A204
- Portegies Zwart, S. F., McMillan, S. L. W., & Gieles, M. 2010, *Annual Review of Astronomy and Astrophysics*, 48, 431
- Prieto, J. L. & Gnedin, O. Y. 2008, *The Astrophysical Journal*, 689, 919
- Puzia, T. H., Paolillo, M., Goudfrooij, P., et al. 2014, *The Astrophysical Journal*, 786, 78
- Rafelski, M. & Zaritsky, D. 2005, *The Astronomical Journal*, 129, 2701
- Rafikov, R. R. 2001, *MNRAS*, 323, 445
- Ramírez-Alegria, S., Borissova, J., Chené, A. B., et al. 2014, *Astronomy & Astrophysics*, 564, L9
- Randriamanakoto, Z., Väisänen, P., Ryder, S. D., & Ranaivomanana, P. 2019, *MNRAS*, 482, 2530
- Reina-Campos, M., Gnedin, O. Y., Sills, A., & Li, H. 2024, arXiv e-prints, arXiv:2408.04694
- Reina-Campos, M., Hughes, M. E., Kruijssen, J. M. D., et al. 2020, *MNRAS*, 493, 3422
- Reina-Campos, M., Keller, B. W., Kruijssen, J. M. D., et al. 2022a, *MNRAS*, 517, 3144
- Reina-Campos, M. & Kruijssen, J. M. D. 2017, *MNRAS*, 469, 1282
- Reina-Campos, M., Kruijssen, J. M. D., Pfeffer, J. L., Bastian, N., & Crain, R. A. 2019, *MNRAS*, 486, 5838
- Reina-Campos, M., Sills, A., & Bichon, G. 2023a, *MNRAS*, 524, 968
- Reina-Campos, M., Trujillo-Gomez, S., Deason, A. J., et al. 2022b, *MNRAS*, 513, 3925
- Reina-Campos, M., Trujillo-Gomez, S., Pfeffer, J. L., et al. 2023b, *MNRAS*, 521, 6368
- Renaud, F. 2018, *New Astronomy Reviews*, 81, 1
- Renaud, F., Gieles, M., & Boily, C. M. 2011, *MNRAS*, 418, 759
- Rodruck, M., Charlton, J., Borthakur, S., et al. 2023, *MNRAS*, 526, 2341
- Romeo, A. B. & Wiegert, J. 2011, *MNRAS*, 416, 1191
- Rosolowsky, E. & Blitz, L. 2005, *The Astrophysical Journal*, 623, 826
- Rostami-Shirazi, A., Zonoozi, A. H., Hagh, H., & Rabiee, M. 2024, *MNRAS*, 535, 3489
- Ryon, J. E., Adamo, A., Bastian, N., et al. 2014, *The Astronomical Journal*, 148, 33
- Ryon, J. E., Bastian, N., Adamo, A., et al. 2015, *MNRAS*, 452, 525
- Ryon, J. E., Gallagher, J. S., Smith, L. J., et al. 2017, *The Astrophysical Journal*, 841, 92
- Safronov, V. S. 1960, *Annales d'Astrophysique*, 23, 979
- Saha, K., tseng, Y.-H., & Taam, R. E. 2010, *The Astrophysical Journal*, 721, 1878
- Salmon, B., Coe, D., Bradley, L., et al. 2018, *The Astrophysical Journal Letters*, 864, L22
- Sánchez-Menguiano, L., Sánchez, S. F., Kawata, D., et al. 2016, *The Astrophysical Journal Letters*, 830, L40
- Sánchez-Menguiano, L., Sánchez, S. F., Pérez, I., et al. 2018, *Astronomy & Astrophysics*, 609, A119
- Sanders, R. L., Shapley, A. E., Jones, T., et al. 2021, *The Astrophysical Journal*, 914, 19
- Sattari, Z., Mobasher, B., Chartab, N., et al. 2023, *The Astrophysical Journal*, 951, 147
- Schaller, G., Schaerer, D., Meynet, G., & Maeder, A. 1992, *Astronomy & Astrophysics Supplement Series*, 96, 269
- Schaye, J., Crain, R. A., Bower, R. G., et al. 2015, *Monthly Notices of the Royal Astronomical Society*, 446, 521
- Schuster, K. F., Kramer, C., Hirschfeld, M., Garcia-Burillo, S., & Mookerjee, B. 2007, *Astronomy & Astrophysics*, 461, 143
- Sesto, L. A., Faifer, F. R., Smith Castelli, A. V., Forte, J. C., & Escudero, C. G. 2018, *MNRAS*, 479, 478
- Shibuya, T., Ouchi, M., Kubo, M., & Harikane, Y. 2016, *The Astrophysical Journal*, 821, 72
- Silva-Villa, E. & Larsen, S. S. 2011, *Astronomy & Astrophysics*, 529, A25
- Somerville, R. S. & Davé, R. 2015, *Annual Review of Astronomy and Astrophysics*, 53, 51
- Somerville, R. S., Hopkins, P. F., Cox, T. J., Robertson, B. E., & Hernquist, L. 2008, *MNRAS*, 391, 481
- Spengler, C., Côté, P., Roediger, J., et al. 2017, *The Astrophysical Journal*, 849, 55
- Spina, L., Magrini, L., & Cunha, K. 2022, *Universe*, 8, 87
- Spinoso, D., Bonoli, S., Valiante, R., Schneider, R., & Izquierdo-Villalba, D. 2023, *MNRAS*, 518, 4672
- Spitler, L. R. & Forbes, D. A. 2009, *MNRAS*, 392, L1
- Spitzer, L. 1940, *MNRAS*, 100, 396
- Spitzer, L. 1987, *Dynamical evolution of globular clusters*
- Springel, V., White, S. D. M., Jenkins, A., et al. 2005, *Nature*, 435, 629
- Springel, V., White, S. D. M., Tormen, G., & Kauffmann, G. 2001, *MNRAS*, 328, 726
- Strader, J., Brodie, J. P., Cenarro, A. J., Beasley, M. A., & Forbes, D. A. 2005, *The Astronomical Journal*, 130, 1315
- Straizys, V., Maskoliūnas, M., Boyle, R. P., et al. 2014, *MNRAS*, 437, 1628
- Sun, J., Leroy, A. K., Rosolowsky, E., et al. 2022, *The Astronomical Journal*, 164, 43
- Tanaka, T. & Haiman, Z. 2009, *The Astrophysical Journal*, 696, 1798

- Tonini, C. 2013, *The Astrophysical Journal*, 762, 39
- Toomre, A. 1964, *The Astrophysical Journal*, 139, 1217
- Torrey, P., Vogelsberger, M., Marinacci, F., et al. 2019, *MNRAS*, 484, 5587
- Tremonti, C. A., Heckman, T. M., Kauffmann, G., et al. 2004, *The Astrophysical Journal*, 613, 898
- Trujillo-Gomez, S., Kruijssen, J. M. D., Reina-Campos, M., et al. 2021, *MNRAS*, 503, 31
- Untzaga, J., Bonoli, S., Izquierdo-Villalba, D., Mezcua, M., & Spinoso, D. 2024, *MNRAS*, 13
- Usher, C., Caldwell, N., & Cabrera-Ziri, I. 2024, *MNRAS*, 528, 6010
- Usher, C., Forbes, D. A., Brodie, J. P., et al. 2012, *MNRAS*, 426, 1475
- Usher, C., Forbes, D. A., Spitler, L. R., et al. 2013, *Monthly Notices of the Royal Astronomical Society*, 436, 1172
- van der Kruit, P. C. & Freeman, K. C. 2011, *Annual Review of Astronomy and Astrophysics*, 49, 301
- Vani, A., Ayromlou, M., Kauffmann, G., & Springel, V. 2025, *MNRAS*, 536, 777
- Vanzella, E., Calura, F., Meneghetti, M., et al. 2019, *MNRAS*, 483, 3618
- Vanzella, E., Calura, F., Meneghetti, M., et al. 2017, *MNRAS*, 467, 4303
- Vanzella, E., Claeysens, A., Welch, B., et al. 2023, *The Astrophysical Journal*, 945, 53
- Vazquez-Semadeni, E. 1994, *The Astrophysical Journal*, 423, 681
- Vázquez-Semadeni, J. S. E., Chappell, D., & Passot, T. 1998, *The Astrophysical Journal*, 504, 835
- Veljanoski, J., Ferguson, A. M. N., Mackey, A. D., et al. 2015, *MNRAS*, 452, 320
- Vijayan, A. P., Scott, S. J., Thomas, P. A., et al. 2019, *MNRAS*, 489, 4072
- Villaume, A., Romanowsky, A. J., Brodie, J., & Strader, J. 2019, *The Astrophysical Journal*, 879, 45
- Wang, E., Wang, H., Mo, H., et al. 2018, *The Astrophysical Journal*, 864, 51
- Wang, K. & Peng, Y. 2024, *Astronomy & Astrophysics*, 12
- Watson, G. N. 1944, *A Treatise on the Theory of Bessel Functions*, *The Mathematical Gazette* (Cambridge University Press)
- Webb, J. J., Harris, W. E., & Sills, A. 2012, *The Astrophysical Journal Letters*, 759, L39
- West, M. J., Côté, P., Jones, C., Forman, W., & Marzke, R. O. 1995, *The Astrophysical Journal Letters*, 453, L77
- West, M. J., Côté, P., Marzke, R. O., & Jordán, A. 2004, *Nature*, 427, 31
- Westfall, K. B., Andersen, D. R., Bershady, M. A., et al. 2014, *The Astrophysical Journal*, 785, 43
- White, S. D. M. & Frenk, C. S. 1991, *The Astrophysical Journal*, 379, 52
- White, S. D. M. & Rees, M. J. 1978, *MNRAS*, 183, 341
- Whitmore, B. C., Chandar, R., Bowers, A. S., et al. 2014, *The Astronomical Journal*, 147, 78
- Yates, R. M., Hendriks, D., Vijayan, A. P., et al. 2024, *MNRAS*, 527, 6292
- Yates, R. M., Henriques, B. M. B., Fu, J., et al. 2021, *MNRAS*, 503, 4474
- Yates, R. M., Henriques, B. M. B., Thomas, P. A., et al. 2013, *MNRAS*, 435, 3500
- Yates, R. M., Thomas, P. A., & Henriques, B. M. B. 2017, *MNRAS*, 464, 3169
- Zaritsky, D. 2022, *MNRAS*, 513, 2609
- Zentner, A. R. & Bullock, J. S. 2003, *The Astrophysical Journal*, 598, 49
- Zhang, Q. & Fall, S. M. 1999, *The Astrophysical Journal Letters*, 527, L81
- Zhong, W., Fu, J., Sharma, P., Shen, S., & Yates, R. M. 2023a, *MNRAS*, 519, 4344
- Zhong, W., Fu, J., Shen, S., & Yuan, F. 2023b, *Research in Astronomy & Astrophysics*, 23, 075004
- Zhou, L., Federrath, C., Yuan, T., et al. 2017, *MNRAS*, 470, 4573

## Appendix A: Model variations

We present here additional variations of model parameters that influence the assembly history of  $z = 0$  star cluster populations.

### Appendix A.1: Velocity dispersion of the cold gas

One of the most crucial parameters for modelling the Toomre parameter is the velocity dispersion of the cold gas. As discussed in e.g. Lehnert et al. (2009) and Zhou et al. (2017) there exists substantial scatter in the relationship between the velocity dispersion of the cold gas and the star formation rate surface density (c.f. Equation 14). In our fiducial model we adopted  $\alpha_{\text{cold}}^{\text{fid}} = 5 \text{ km s}^{-1}$ ,  $\beta_{\text{cold}}^{\text{fid}} = 20 \text{ km s}^{-1}$ , and  $\gamma_{\text{cold}}^{\text{fid}} = 1/3$  for the offset, slope, and exponent, respectively.

Here we explore a wider parameter range by testing a first version where we increase the slope value to  $\beta_{\text{cold}}^{\text{var}} = 100 \text{ km s}^{-1}$  and a second version where we set the exponent to  $\gamma_{\text{cold}}^{\text{var}} = 1/2$ . Additionally, we test a separate prescription based on the Jeans mass (see e.g. Elmegreen et al. 2007) where

$$\sigma_{g,j} \sim M_J^{1/4} G^{1/2} \Sigma_{g,j}^{1/4} = 4.4 \text{ pc Myr}^{-1} \times \Sigma_{\text{SFR},j}^{0.18}, \quad (\text{A.1})$$

with  $M_J$  as the Jeans mass, which we assume to be  $10^9 M_\odot$  for the equality, and converted from the cold gas surface density to the star formation rate density using Equation 7 from Kennicutt (1998) with  $\Sigma_{\text{SFR}}$  in units of  $10^6 M_\odot \text{ pc}^{-2} \text{ Myr}^{-1}$ . In addition, we add a velocity floor of  $5 \text{ km s}^{-1}$ , the same value that we used in Equation 14.

To probe the effect of this relationship on the properties of newly formed star clusters, we fit linear relationships to the resulting  $M_V$ -SFR parameter space, as presented in Section 3.1, and present the slope values in Table A.1.

We find that an increase of  $\beta_{\text{cold}}$  results in a steeper slope value of the  $M_V$ -SFR relationship for both dwarf and massive galaxies. This change is a direct consequence of modifications to the Toomre parameter. Since  $Q_{D,g} \propto c_{s,\text{cold}}$ , the Toomre parameter of the gas increases/decreases, which then also results in an increase/decrease of  $Q_{\text{eff}}$ , albeit not as strong as  $Q_{D,g}$  due to taking a weighted average with  $Q_{D,s}$ . This increase/decrease has a direct consequence on the star cluster masses because the upper truncation mass in Equations 28 and 29 scales as  $m_{\text{cl,max}} \propto Q_{\text{eff}}^4$ , resulting in an increased/decreased probability to randomly sample massive clusters.

When modifying the power-law index to  $\gamma_{\text{cold}} = 1/2$  when find a significant increase in the slope value for massive galaxies whereas it is less strong for dwarfs. While the above argument is valid for this case as well, the secondary dependence comes from the galaxy-mass to star formation rate dependency. It can be seen in panel (B) of Figure 4 that more massive galaxies have, on average, higher star formation rates and are, thus, more significantly affected from the change in  $\gamma_{\text{cold}}$ .

Finally, when assuming a prescription based on the Jeans mass we find significantly shallower slopes for the same reasons outlined above. These slopes are also too shallow compared to the observational constraints

Our simulations indicate that the slope of the relationship is steeper for more massive galaxies irrespective of the assumed cold gas velocity dispersion versus surface star formation rate relationship.

Table A.1: Slope values of the  $M_V$ -SFR relationship when adjusting parameters for the  $c_{s,\text{cold}}-\Sigma_{\text{SFR}}$  relationship.

Model	Slope values	
	high-mass	low-mass
Fiducial	$-3.64_{-0.02}^{+0.02}$	$-2.63_{-0.01}^{+0.02}$
$\beta_{\text{cold}}^{\text{var}} = 100 \text{ km s}^{-1}$	$-3.98_{-0.02}^{+0.02}$	$-3.27_{-0.02}^{+0.02}$
$\gamma_{\text{cold}}^{\text{var}} = 1/2$	$-3.73_{-0.02}^{+0.02}$	$-2.70_{-0.02}^{+0.02}$
$c_{s,\text{cold}} \propto (M_J \Sigma_g)^{1/4}$	$-2.32_{-0.01}^{+0.01}$	$-1.31_{-0.02}^{+0.02}$

### Appendix A.2: Initial half-mass radius

The distribution of initial half-mass radii remains an unsolved problem. Measurements of the half-light size of young star clusters give typical values in the range of a few parsecs to about 0.5 pc (e.g. Bastian et al. 2012; Ryon et al. 2015; Brown & Gnedin 2021) but the scatter at similar cluster ages is large, going up to  $\approx 20$  pc for W 3 in NGC 7252 (Maraston et al. 2004; Fellhauer & Kroupa 2005). This could indicate that the initial half-mass radius of clusters is similar and diverges due to a different initial evolutionary phase given the local environment, or that other parameter influence the initial half-mass radius, such as cluster mass or the local physical conditions. Reina-Campos et al. (2023a) tested different prescriptions of initial half-mass radii, considering constant values, constant densities, a linear relationships from the data provided by Brown & Gnedin (2021), and a theoretical model from Choksi & Kruijssen (2021) that reads

$$r_{c,h} = \left( \frac{3}{10\pi^2} \frac{\alpha_{\text{vir}}}{\phi_P \phi_{\bar{P},j}} \frac{m_c^2}{\Sigma_g^2} \right)^{1/4} \frac{\epsilon_c^{1/2}}{2\epsilon_c - 1} \frac{f_{\text{acc}}}{Q_{\text{eff}}^2}, \quad (\text{A.2})$$

with  $f_{\text{acc}} = 0.6$ ,  $\epsilon_c = 1.0$ , and environmentally-dependent parameters evaluated for each ring.<sup>10</sup> Reina-Campos et al. (2023a) conclude that none of the prescriptions reproduce the size-mass relationship after evolving the cluster population for a few Gyr within the *EMP-Pathfinder* simulation suite (Reina-Campos et al. 2022a).

Similar to Reina-Campos et al. (2023a) we implement different prescriptions for the initial half-mass radius, that we outline in Table A.2, to test their influence on the stellar mass versus size distribution at  $z = 0$ , as discussed in Section 3.2. We find that the precise details of the initial half-mass radius clearly change the resulting distribution of young star clusters, however, the distribution of radii of old star clusters remain largely unchanged. The greatest differences compared to the fiducial model are for a constant  $r_{c,h} = 0.1 \text{ pc}$  and the empirical relationship where  $r_{c,h} \propto m_c^{0.18}$ . The compact initial size of star clusters results in the most massive star clusters to rapidly expand up to 30 pc, values that are not reached with other prescriptions. The increased half-mass radius of the empirical relationship causes an apparent impact on the size of old star clusters

<sup>10</sup> The parameter  $\epsilon_c$  refers to the efficiency of star formation within a giant molecular cloud and not the average efficiency of star formation within the interstellar medium that was introduced in Section 2.3.3.

Table A.2: Variations in the initial half-mass radii of star clusters.

Model	Prescription
Fiducial	$r_{c,h} = 1.0 \text{ pc}$
Compact	$r_{c,h} = 0.1 \text{ pc}$
Density	$r_{c,h} = 1 \text{ pc} \times (m_c/10^4 M_\odot)^{0.3}$
Empirical <sup>(a)</sup>	$r_{c,h} = 2.37 \text{ pc} \times (m_c/10^4 M_\odot)^{0.18}$
Theoretical <sup>(b)</sup>	$r_{c,h} \propto \sqrt{m_c/\Sigma_g}$

<sup>(a)</sup> Fitting results provided by [Reina-Campos et al. \(2023a\)](#) for the data of [Brown & Gnedin \(2021\)](#) when limiting the star cluster population to ages  $1 \text{ Myr} \leq \tau_c \leq 10 \text{ Myr}$ .

<sup>(b)</sup> Adopted from [Choksi & Kruijssen \(2021\)](#). To avoid extremely compact or extended clusters we introduce a lower and upper boundary to a star cluster's half-mass radius of 0.1 and 100 pc, respectively.

within the galactic disk as well: on average, the star clusters in a disk become larger by two to three parsecs.

Overall, we find that the precise prescription of the initial half-mass radius does not significantly impact the results at  $z = 0$ .

### Appendix A.3: Cluster initial mass function

To test the effect of the upper truncation mass on the resulting star cluster populations we re-run the model considering a pure power-law cluster initial mass function, i.e.  $\xi(m_c) \propto m_c^\alpha$ . Similar to the fiducial model we pre-compute a list of  $10^6$  random realisations of this mass function between  $10^2$  and  $10^8 M_\odot$  and randomly sample it to reduce computational cost.

The overall shape and distribution of the half-mass radii remain unchanged. A significant difference occurs at the high-mass end of the mass distribution, which is much more densely populated. This change impacts the data points on the  $M_V$ -SFR relationship by shifting them to lower absolute magnitudes, resulting in a steeper relationship when compared to both the fiducial model and observations. The model then also fails to account for the faintest young star clusters in galaxies above star formation rates above  $\approx 1 M_\odot \text{ yr}^{-1}$ .

In the *E-MOSAICS* simulation [Pfeffer et al. \(2023\)](#) find that the median metallicity values of star clusters in dwarf galaxies is elevated by 0.2 to 0.4 dex, depending on galaxy mass (their Figure 7). In our simulation we find a difference of about 0.2 dex below galaxy stellar masses of  $M_\star \approx 8 \times 10^9 M_\odot$ , which is in excellent agreement with the results by [Pfeffer et al. \(2023\)](#). At higher galaxy masses we see no change in the distribution between the two models likely reflecting that the upper truncation mass was high enough at typical star cluster formation redshifts (see e.g. Figure 8 in [Pfeffer et al. 2018](#)). We will investigate the redshift-dependence of our model parameters in future efforts.